



OPEN Revealing various change characteristics and drivers of ecological vulnerability in the Luan river basin based on the SRP model

Yang Li^{1,2✉}, Wenquan Xie³, Kelin Sui^{1,2}, Dongming Zhang^{1,2✉} & Qian Wan⁴

As a vital ecological barrier and water source for the Beijing-Tianjin-Hebei (BTH) region, the Luan River Basin (LRB) plays a crucial role in maintaining regional ecological balance. However, comprehensive research on Ecological Vulnerability (EV) evaluation in the LRB remains scarce, making EV evaluation and forecasting particularly significant. This study evaluated EV dynamics (2002–2022) via the SRP model with 17 indicators, with driving factors analyzed via Geodetector and 2032 scenarios forecasted by CA-Markov. Key findings revealed: (1) EVI increased from 0.397 to 0.428 (peak at 0.445 in 2017), with Microscopic vulnerability dominating (46.47% average area). (2) Spatially, EV exhibited a “low-medium-high” gradient (lower in northwestern high-altitude areas and higher in southeastern plains), confirmed by significant clustering (Global Moran's $I = 0.889\text{--}0.938$, p value < 0.001). (3) Geodetector identified elevation ($q = 0.855$), biological abundance ($q = 0.812$), annual temperature ($q = 0.800$), and cultivated land proportion ($q = 0.783$) as primary driving factors. (4) CA-Markov forecasts for 2032 indicate declines in Potential vulnerability (-5.83%), Microscopic vulnerability (-2.01%), and Severe vulnerability (-2.30%), but increases in Mild vulnerability ($+6.57\%$) and Moderate vulnerability ($+3.57\%$). These findings provide a scientific basis for evidence-based ecological policies in the LRB, contributing to the promotion of regional sustainable development and the balance between ecological conservation and economic growth.

Keywords Ecological vulnerability, Luan river basin, SRP model, CA-Markov model, Geodetector, Ecological policy

The ecological environment, a complex network of living and non-living components, sustains biodiversity and human well-being through critical functions like climate regulation and habitat provision^{1,2}. Ecological Vulnerability (EV)—the susceptibility of ecosystems to disturbances and their recovery capacity³—guides environmental management and sustainable development⁴. The EV research originated in the 1960s, initially focusing on ecosystem responses to natural disasters⁵. Since then, the field has expanded significantly, with researchers worldwide recognizing the multifaceted nature of EV. International collaborations, such as those under the Intergovernmental Panel on Climate Change (IPCC), have highlighted the global significance of EV in the context of climate change and its implications for human societies⁶, and research has shifted from isolated analyses to interdisciplinary integration, reflecting ecological complexity.

As research progresses, several models for evaluating EV have been developed, including the Pressure-State-Response (PSR) model, Exposure-Sensitivity-Adaptability (ESA) model, and Sensitivity-Resilience-Pressure (SRP) model, among others⁷. Among these models, the PSR model focuses on ecosystem responses to pressures from human activities⁸, while the ESA model places greater emphasis on the extent to which ecosystems or ecosystem components are actually exposed to specific stressors⁹. In contrast to the aforementioned models, the SRP model—based on a social-natural coupled system—offers advantages such as a comprehensive evaluation framework and well-developed indicators. It can more fully capture the integrated characteristics of EV. Therefore, the SRP model was applied to evaluate EV in this study^{7,10–12}.

¹Langfang Integrated Natural Resources Survey Center, China Geological Survey, Langfang 065000, China.

²Innovation Base for Natural Resources Monitoring Technology of Yongding River Downstream Areas, Geological Society of China, Langfang 065000, China. ³School of Geographic Sciences, Xinyang Normal University, Xinyang 464000, China. ⁴Henan Science and Technology Innovation Center of Natural Resources (Application Research of Information Perception Technology), Zhengzhou 450000, China. ✉email: liyang1112@mail.cgs.gov.cn; zhangdongming@mail.cgs.gov.cn

Determining indicator weights in EV evaluation is a crucial step, including mainstream methods such as the Analytic Hierarchy Process (AHP), Entropy Weight Method, Spatial Principal Component Analysis (SPCA), and Fuzzy Comprehensive Evaluation Method¹³. Each method has its advantages: AHP relies on expert judgment, the Entropy Weight Method is favored for its simplicity and objectivity, and the Fuzzy Comprehensive Evaluation Method excels at handling fuzzy and uncertain information. In comparison, this study selected the SPCA⁹ because it can effectively reduce data dimensionality and objectively allocate weights through variance contribution rates, retaining the main information of the data while reducing human intervention.

The SRP model has been widely applied across regions. For instance, Zou et al. used it to establish an EV evaluation system and analyze spatiotemporal characteristics (2000–2018) by combining AHP and PCA to calculate weights in Jilin Province¹⁴. He et al. combined it with Geodetector to reveal EV dynamics and driving mechanisms of EV in Yunnan Province¹. Li et al. applied it in Liaoning, integrating Geodetector and CA-Markov for driver analysis and trend forecasting¹⁵. Zhang et al. applied it to evaluate EV in the Yellow River Basin, analyzed how ecological restoration measures affect EV changes, and highlighted the interaction between human activities and the ecological environment¹⁶.

The Luan River, originating in Fengning County, flows through Hebei, Liaoning, and the Inner Mongolia Autonomous Region before discharging into the Bohai Sea at Laoting County. Its basin serves as an essential ecological barrier to mitigate the impact of dust storms from Mongolia on the North China region and is a vital water resource for the Beijing-Tianjin-Hebei (BTH) area. Previous studies on the Luan River Basin (LRB) have been conducted. For instance, Yang et al. assessed the spatiotemporal characteristics and driving factors of landscape ecological risk in the LRB¹⁷. Liu et al. studied the distribution and accumulation of heavy metals in the water and evaluated the associated ecological risks¹⁸. However, critical knowledge gaps persist in current LRB studies: (1) Spatiotemporal dynamics of EV remain unquantified, with limited analysis of long-term evolution patterns (e.g., gradient shifts, centroid migration). (2) Future trajectory projections are absent, hindering proactive policy formulation. (3) Existing evaluations lack integration of multi-dimensional drivers.

To address these gaps, this study employed the SRP model with 17 natural and anthropogenic indicators, SPCA for weighting, to calculate and classify the Ecological Vulnerability Index (EVI, the quantitative expression of EV) for the LRB (2002–2022). We analyze EVI's spatiotemporal patterns via Moran's I, identify drivers with Geodetector, and forecast future EV using CA-Markov. Findings aim to support regional ecological policy-making.

Materials and methods

Study area

The Luan River is one of the significant rivers in North China (as shown in Fig. 1), and it originates from Fengning Manchu Autonomous County in Hebei Province. It flows through Hebei, Liaoning, and Inner Mongolia, with a total length of approximately 888 km and a basin area of about 53,100 square kilometers. The terrain of the LRB is complex and varied; the upper reaches are situated on the Bashang Plateau, the middle reaches pass through the Yanshan mountain range, and the lower reaches traverse the Hebei Plain to the Bohai Bay. There is a considerable variation in terrain within the basin, with the land sloping from the northwest to the southeast. The average annual temperature and precipitation across the basin are 7.0 ± 2.6 °C and 488.4 ± 80.7 mm¹⁹, respectively, exhibiting a distinct heterogeneous seasonal distribution, with the main wet season occurring in July and August each year²⁰.

The LRB is a vital industrial base for the BTH region, including important industrial cities such as Tangshan and Qinhuangdao. It also plays a crucial role in ecological support and water conservation for the region²¹.

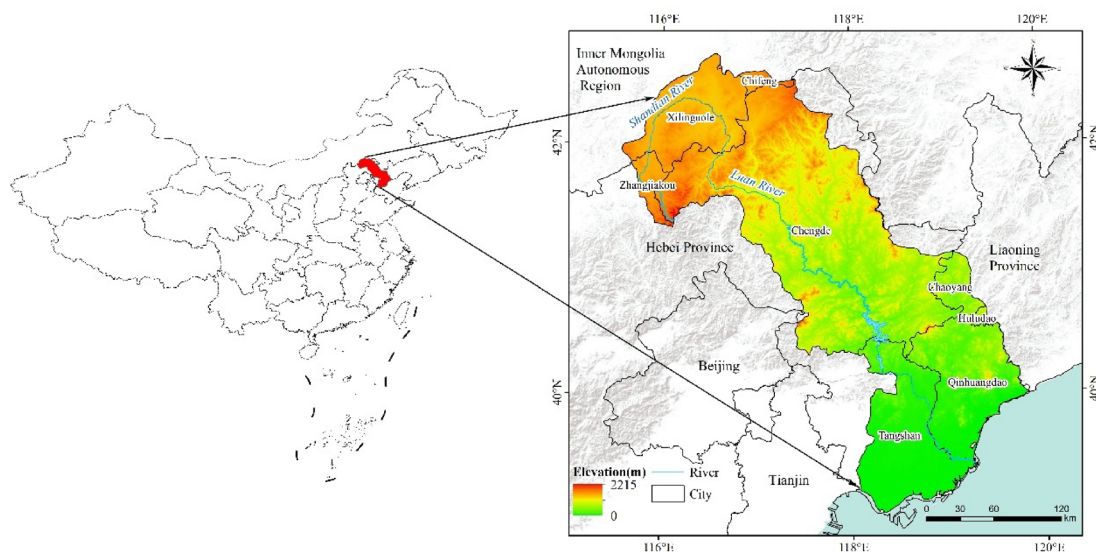


Fig. 1. Location of the study area.

However, with the rapid economic development in recent years, unreasonable land use, extensive construction of water conservancy projects, and over-extraction of groundwater have led to environmental issues such as soil erosion, river runoff decreasing, wetland reduction, and loss of biodiversity within the basin^{22–24}. Therefore, analyzing the spatiotemporal patterns of EV in the LRB, uncovering its driving factors, and forecasting its future development are of significant importance for the formulation of policies aimed at the construction of ecological civilization in the basin.

Data and pre-processing

Considering the availability of data and the process of urban development, in order to comprehensively reflect the pattern of changes in the EV of the LRB over the past two decades, this study selected the period from 2002 to 2022 as the research timeframe, with a time interval of five years. The data utilized in this study included the Digital Elevation Model (DEM)²⁵, remote sensing imagery^{26,27}, soil data²⁸, meteorological data^{29,30}, land use types³¹, basic geographical information (including residential points, road networks, and water networks)³², and population data³³. To ensure spatial consistency across all datasets, these datasets were processed through cropping, projection, and resampling. A uniform spatial reference system, WGS 1984 UTM Zone 50N, was used, with a spatial resolution of 1 km. The sources of the data and the methods of preprocessing were shown in Table 1.

Methods

Research technique route

Based on the SRP model, this study selected 17 indicators that can measure EV from different perspectives within the three dimensions of ecological sensitivity, ecological resilience, and ecological pressures. The study calculated the weights of each indicator by SPCA and constructed an EVI map to analyze its spatiotemporal characteristics. Global and local autocorrelation tools were employed to explore the spatial heterogeneity of EV in the study area, and Geodetector was used to analyze the driving factors. Finally, the CA–Markov model was applied to forecast the future EV of the study area based on the existing data outcomes. The research technique route of this study is illustrated in Fig. 2.

This integrated method fully utilizes the advantages of each approach: SPCA assigns objective weights to SRP indicators. Geodetector reveals driving mechanisms comprehensively. CA–Markov combines spatial adjacency rules with transition probabilities to forecast future scenarios. This synergy enables a comprehensive diagnosis of EV spatiotemporal patterns and overcomes the limitations of single-method studies.

Establishment of evaluation index system

This study, based on the SRP model, comprehensively and objectively established an EV evaluation index system for the LRB, taking into account the natural environment and human activity characteristics of the basin. In line with relevant research^{10,14,15,37}, and adhering to principles of scientificity, representativeness, and data accessibility, the indicators were grounded in data related to topography, soil, climate, vegetation, ecological vitality, landscape patterns, and human activities. The details were shown in Table 2.

Ecological sensitivity refers to the susceptibility of ecosystems to internal and external disturbances¹⁰, including topographic factors (elevation, slope, and terrain roughness), meteorological factors (annual average precipitation, annual average temperature, and rainfall erosivity factor R), and soil factors (soil erodibility factor K). Ecological resilience refers to the ability of ecosystems to self-regulate and self-repair after disturbances, which is related to the internal structure of the ecosystem, including landscape structure (Shannon diversity index), ecological vitality (biological abundance), natural conditions (water network density), and vegetation status (NDVI and NPP). Ecological pressure refers to the degree to which ecosystems are affected by external disturbances and impacts, usually caused by human activity factors (cultivated land proportion, construction land proportion, residential point kernel density, population density, and road network density).

Name	Data source	Time	Resolution /scale	Pre-processing
Annual average precipitation	http://data.tpdc.ac.cn/	2002–2022	1 km	Image cropping, calculating rainfall erosivity factor r^{34} in ArcGIS based on the RUSLE model
Annual average temperature	http://data.tpdc.ac.cn/	2002–2022	1 km	Image cropping
DEM	https://www.gscloud.cn/	–	30 m	calculating slope and terrain ruggedness Index in ArcGIS
Soil	http://data.tpdc.ac.cn/	–	1:1,000,000	Calculating soil erodibility factor K^{35} in ArcGIS based on the RUSLE model
Net primary productivity (NPP)	http://www.gis5g.com	2002–2022	500 m	Resampling
Normalized difference vegetation Index (NDVI)	http://www.gisrs.cn	2002–2022	500 m	Resampling
Basic geographic information	https://www.ngcc.cn/	–	1:250,000	Calculating residential point kernel density, road network density, and water network density in ArcGIS
Population density	https://landscan.ornl.gov/	2002–2022	1 km	Image cropping
Land use type	https://zenodo.org/	2002–2022	30 m	Calculating shannon diversity Index in fragstats and biological abundance ³⁶ , cultivated land proportion, and construction land proportion in ArcGIS

Table 1. The data sources and pre-processing.

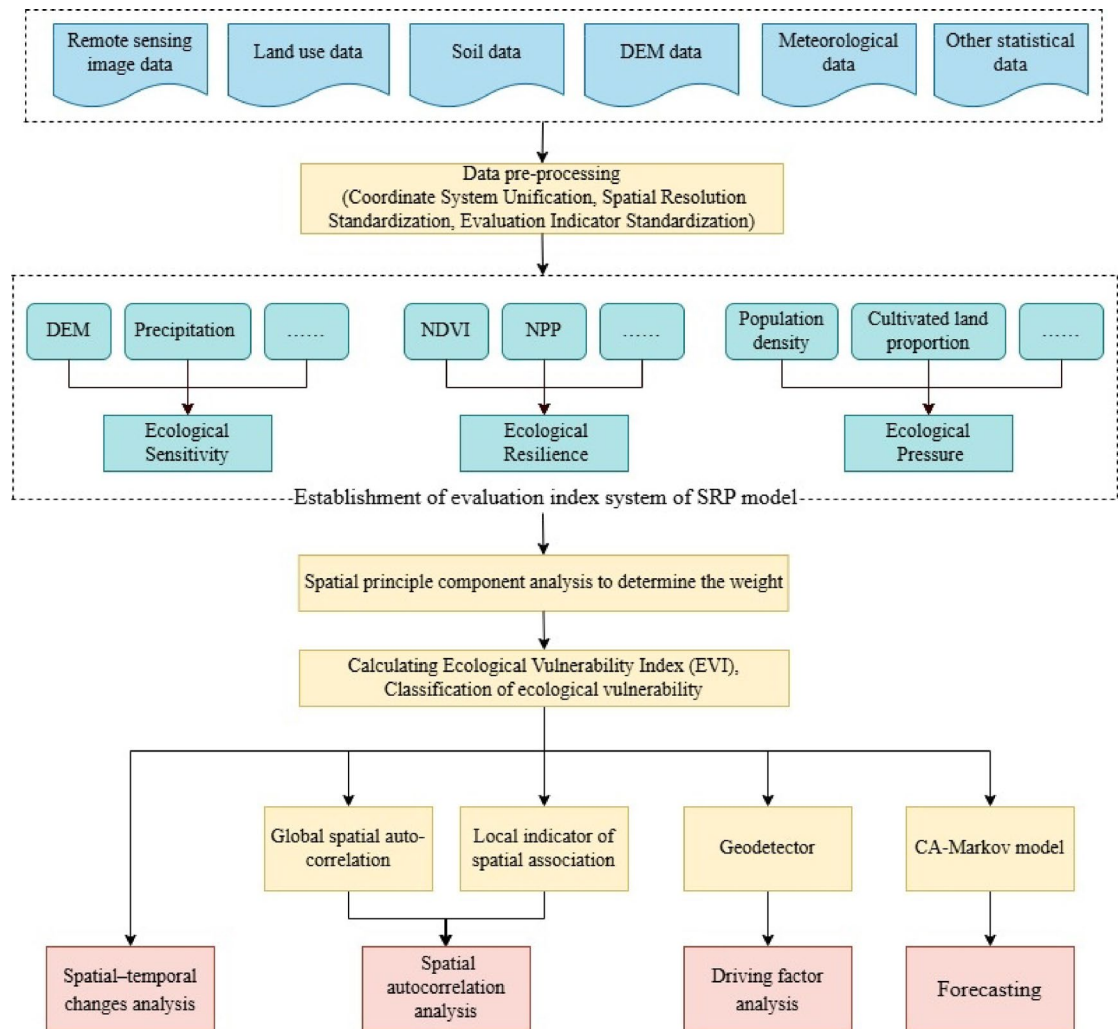


Fig. 2. Research technology roadmap.

Criterion Layer	Indicators	Attribute	Indicator significance
Ecological sensitivity	Elevation (X1)	Negative	High-altitude areas have less human activity in the study area
	Slope (X2)	Positive	Affects soil erosion, water flow velocity, and sediment distribution
	Terrain Ruggedness Index (X3)	Positive	Prone to soil erosion and land degradation
	Annual average precipitation (X4)	Negative	Precipitation can affect vegetation growth
	Annual average temperature (X5)	Negative	Temperature affects the growth and reproduction of organisms
	Soil erodibility factor K (X6)	Positive	Influences the condition of soil erosion
	Rainfall Erosivity factor R (X7)	Positive	Reflects the potential erosive action of rainfall on soil
Ecological resilience	Normalized vegetation Index (X8)	Negative	Reflects the degree of surface vegetation cover
	Biological abundance (X9)	Negative	Reflects the number, variety, and distribution of species within an ecosystem
	Net primary productivity (X10)	Negative	Related to energy transformation and material cycling
	Water network density (X11)	Negative	Directly affects the health of surrounding ecosystems
	Shannon diversity Index (X12)	Negative	Reflects landscape diversity
Ecological pressure	Residential Point Kernel Density (X13)	Positive	Human settlement range exerts pressure on the surrounding environment
	Road Network Density (X14)	Positive	Reflects the extent of human activity and its pressure on the environment
	Cultivated Land Proportion (X15)	Positive	Related to biodiversity and ecosystem stability
	Construction Land Proportion (X16)	Positive	Urban expansion may lead to the destruction of natural ecosystems
	Population Density (X17)	Positive	Reflects the pressure of the population on resource utilization and the environment

Table 2. Ecological vulnerability evaluation indicator system.

Establishment of EVI

Standardization of evaluation indicators

Due to the differences in dimensions and attributes among various indicators, it was necessary to standardize them before conducting EV analysis and evaluation, unifying their value ranges within [0–1]³⁸. The standardization formulas for positive and negative indicators were shown in Eqs. (1) and (2), respectively.

$$Z_{i,positive} = \frac{x_i - x_{i,min}}{x_{i,max} - x_{i,min}} \quad (1)$$

$$Z_{i,negative} = \frac{x_{i,max} - x_i}{x_{i,max} - x_{i,min}} \quad (2)$$

where $Z_{i,positive}$ represents the positive standardized value of the i -th indicator, $Z_{i,negative}$ represents the negative standardized value of the i -th indicator, x_i is the raw value of the i -th indicator, $x_{i,max}$ is the maximum value of the i -th indicator, $x_{i,min}$ is the minimum value of the i -th indicator.

Spatial principal component analysis

Unlike subjective weighting methods (e.g., AHP), SPCA objectively determines weights based on variance contribution rates. It allows for the retention of as much information reflected by a larger set of original indicators through a smaller set of comprehensive indicators, and it effectively mitigates the influence of human factors, thereby enhancing the objectivity of the evaluation³⁹. In this study, after standardizing the indicators, we applied SPCA and retained the first seven principal components (Table 4) since their cumulative contribution rate exceeded 90% in all years included in the study. These components were then used to calculate the EVI via weighted integration as shown in Eq. (3).

$$I_{EVI} = \alpha_1 Y_1 + \alpha_2 Y_2 + \alpha_3 Y_3 + \cdots + \alpha_n Y_n \quad (3)$$

where I_{EVI} represents the EVI, α_n denotes the contribution rate of the n -th principal component, Y_n signifies the n -th principal component.

To facilitate the comparison of EVI across different periods, it was necessary to standardize them, as shown in Eq. (4).

$$SEVI_i = \frac{EVI_i - EVI_{i,min}}{EVI_{i,max} - EVI_{i,min}} \quad (4)$$

where $SEVI_i$ represents the standardized value of EVI for the i -th year, $EVI_{i,max}$ denotes the maximum value of the EVI for the i -th year, $EVI_{i,min}$ signifies the minimum value of the EVI for the i -th year.

Additionally, the EVI of the LRB was categorized into five levels: Potential vulnerability [0–0.2), Microscopic vulnerability [0.2–0.4), Mild vulnerability [0.4–0.6), Moderate vulnerability [0.6–0.8), and Severe vulnerability [0.8–1].

Centroid transfer model

The trajectory of the centroid migration can directly reveal the distributional changes of EV throughout the specified timeframe⁴⁰. The trajectory's direction signifies the spatial transformation's orientation and tendency of EV, and the distance indicates the level of dynamism in EV's spatial redistribution. The centroid coordinates can be expressed in Eqs. (5) and (6) below.

$$X_t = \frac{\sum_{i=1}^n (C_{ti} \times X_{ti})}{\sum_{i=1}^n C_{ti}} \quad (5)$$

$$Y_t = \frac{\sum_{i=1}^n (C_{ti} \times Y_{ti})}{\sum_{i=1}^n C_{ti}} \quad (6)$$

where X_t and Y_t represent the centroid coordinates within the EV classification range for the year t ; n is the number of pixels within the EV classification range, C_{ti} is the EVI for pixel i in the year t , X_{ti} and Y_{ti} are the geometric center coordinates of pixel i in year t respectively.

Spatial correlation analysis

In this study, to investigate the patterns of spatial aggregation of EV in the LRB, we utilized the spatial autocorrelation analysis module within the GeoDa 1.20 (<https://spatial.uchicago.edu/geoda>) software to examine the spatial correlation characteristics of the study area. This research calculated the Global Moran's I and Local Moran's I indices for EV in the LRB from 2002 to 2022. Moran's I index serves as a statistical measure that assesses the degree of spatial autocorrelation, or clustering, of a variable across different scales. The Global Moran's I was employed to ascertain whether there is a spatial clustering relationship concerning EV within the LRB. In contrast, the Local Moran's I was applied to evaluate the specific patterns of spatial aggregation of EV in the basin. Through these measurements, the study aimed to offer a comprehensive analysis of the spatial distribution and clustering tendencies of EV over the designated period.

Global spatial autocorrelation.

Global spatial autocorrelation was primarily used to describe the spatial distribution and clustering characteristics of a particular attribute within the entire study area⁴¹. And its calculation formula was presented in Eq. (7) below.

$$I_1 = \frac{n \sum_{i=1}^n \sum_{j=1}^n w_{ij} (x_i - \bar{x})(x_j - \bar{x})}{\sum_{i=1}^n \sum_{j=1}^n w_{ij} \sum_{k=1}^n (x_k - \bar{x})^2} \quad (7)$$

where I_1 represents the Global Moran's I index, n denotes the number of spatial grid cells, w_{ij} signifies the spatial weight matrix, x_i and x_j correspond to the values of the EVI for the i -th and j -th grid cells respectively, \bar{x} indicates the mean value of the EVI across the grid cells. The Moran's I index ranges from -1 to 1. When the index value is greater than 0, it indicates that the attribute exhibits a state of spatial aggregation; when it is less than 0, it suggests that the attribute is in a state of spatial dispersion; and when it tends towards 0, it implies that the attribute is randomly distributed in space.

Local spatial autocorrelation.

The Local Indicators of Spatial Association (LISA) was primarily used to reflect the degree of correlation between a local area and its neighboring areas⁴². And its calculation formula was expressed in Eq. (8) below.

$$I_2 = \frac{n (x_i - \bar{x}) \sum_j w_{ij} (x_j - \bar{x})}{\sum_i (x_i - \bar{x})^2} \quad (8)$$

where I_2 represents the Local Moran's I index; the meanings of the other indicators are the same as those in Eq. (7). The spatial clustering patterns are categorized as "HH" for high-high clusters, "HL" for high-low clusters, "LH" for low-high clusters, "LL" for low-low clusters and not significant.

Driving factors detection

The Geodetector is a powerful tool for measuring, exploring, and leveraging spatial heterogeneity⁴³. At its theoretical core, it identifies the consistency of spatial distribution patterns between the dependent and independent variables through spatial heterogeneity, thereby assessing the impact of the independent variables on the dependent variable⁴⁴. In this study, we created a grid of 1 km by 1 km cells, totaling 53,194 points, for the extraction of both independent and dependent variables.

The choice of different discrete combinations of independent variables has a significant impact on the analysis of driving factors. Song et al. regarded the combination with the maximum q value as the optimal discretization parameter for continuous factors and integrated the Optimal Parameters-based Geographical Detector (OPGD) model into the "GD" package in R⁴⁵. In our analysis of driving factors, we employed the OPGD model and adopted five classification methods (such as equal interval classification, natural breaks classification, standard deviation classification, geometric interval classification, and quantile classification) with the number of categories set between 3 and 8. By calculating the q statistic for each continuous factor under different classification methods and category numbers, we selected the parameter combination (classification method + number of categories) with the highest q value as the optimal parameters for the best discretization treatment of continuous factors⁴⁶.

This approach aims to reveal the driving mechanisms of EV from the perspective of spatial differentiation. The Geodetector is comprised of four main components: The factor detector, the interaction detector, the risk zone detector, and the ecological detector. In this study, the factor detector and the interaction detector were used.

The factor detector was used to detect the ability of the independent variable X to explain the dependent variable Y , measured by the q -value. The formula was shown in Eq. (9) below.

$$q = 1 - \frac{\sum_{h=1}^L N_h \sigma_h^2}{N \sigma^2} = 1 - \frac{SSW}{SST} \quad (9)$$

where: $h = 1, L$ is the stratification of the variable Y or the factor X , N_h and N are the number of cells in stratum h and in the whole region, respectively, σ_h^2 and σ^2 are the variance of the Y values in stratum h and in the whole region, respectively. SSW and SST are the sum of the variances within the stratum and the total variance in the whole region, respectively. The q value ranges from 0 to 1, the closer the value of q is to 1, the greater the explanatory power of the independent variable X on the dependent variable Y , and vice versa.

The Interaction detector was used to detect whether different factors X interact with each other or whether the factors are independent of each other. The types of interactions were classified into the following five types, as shown in Table 3.

Forecasting EV based on CA-markov model

In this study, the CA-Markov model was used to simulate and forecast the EV of the LRB in the year 2032⁴⁷. Cellular Automata (CA) consist of discrete cells in terms of time, space, and state, which simulate the process of spatiotemporal evolution through a certain set of transition rules. This model possesses strong capabilities in spatial computation and simulation, making it particularly suitable for the dynamic simulation and spatial visualization of self-organizing functional systems. The formulation was represented as shown in Eq. (10).

$$S_{ij}^{t+1} = f_q(S_{ij}^t) \quad (10)$$

Basis for judgment	Types of interaction
$q(X1 \cap X2) < \text{Min}(q(X1), q(X2))$	Nonlinear weakening
$\text{min}(q(X1), q(X2)) < q(X1 \cap X2) < \text{Max}(q(X1), q(X2))$	Single-factor nonlinearity weakening
$q(X1 \cap X2) > \text{Max}(q(X1), q(X2))$	Two-factor enhancement
$q(X1 \cap X2) = q(X1) + q(X2)$	Independent
$q(X1 \cap X2) > q(X1) + q(X2)$	Nonlinear enhancement

Table 3. Types of interactive detection.

where S_{ij}^t represents the state of the cell at position (i, j) at time t, f_q is the cell transition function, and S_{ij}^{t+1} represents the state of the cell at position (i, j) at time t + 1.

The principle of the Markov model is to forecast the trend of changes at time t + 1 by utilizing the transition probabilities between the initial state and the intermediate state at time t. Essentially, it is about forecasting the probabilities of events occurring. The transition matrix numerically reflects the likelihood of an event transitioning from state t to state t + 1, and it serves as a crucial quantitative foundation for simulation and forecasting outcomes within the Markov model. The formulation was represented as shown in Eq. (11).

$$S^{t+1} = S^t \times P \tag{11}$$

where P is a state transition matrix, and its formula was expressed in Eq. (12).

$$P = \begin{bmatrix} P_{11} & \cdots & P_{1n} \\ \vdots & \ddots & \vdots \\ P_{n1} & \cdots & P_{nn} \end{bmatrix} \tag{12}$$

The CA–Markov model leverages the strengths of both the CA model in simulating spatial system dynamics and the Markov model in long-term forecasting. It adeptly performs spatiotemporal simulations of EV, addressing both quantitative and spatial aspects, while mitigating the occurrence of random distributions during the simulation, thus enhancing the precision of the model⁴⁸. In this study, we employed the CA–Markov model within the IDRISI Selva 17 software (<http://www.clarklabs.org>) to forecast the EV of the study area for the year 2022, utilizing EV data from the years 2002 and 2012. Subsequently, we used the CROSSTAB tool in the IDRISI Selva 17 software to overlay actual data with the simulated data for 2022, assessing the accuracy of the simulation outcomes and confirming the suitability of the CA–Markov model for EV forecasting. Lastly, based on the EV data from 2012 and 2022, we forecasted the EV status of the study area for the year 2032.

Results
Spatiotemporal differentiation characteristics of EV

As shown in Table 4, SPCA identified the first 7 principal components (cumulative contribution rate > 90%) from the 17 indicators in the LRB ecological vulnerability evaluation system. Then, the EVI was calculated using Eqs. (3) and (4), and classified into five levels: Potential vulnerability, Microscopic vulnerability, Mild vulnerability, Moderate vulnerability, and Severe vulnerability. From 2002 to 2022, the EVI mean values of the study area and the area proportions of each EV level were depicted in Fig. 3.

The EVI mean values for the study area in the years 2002, 2007, 2012, 2017, and 2022 were 0.397, 0.420, 0.407, 0.445, and 0.428, respectively. The minimum value occurred in 2002, and the maximum value occurred in 2017. Over the past 20 years, the EVI of LRB has shown a fluctuating upward trend. Overall, the EV level in LRB is primarily dominated by Microscopic vulnerability, with an average proportion of 46.47%, reaching a maximum of 53.25% in 2002 and a minimum of 41.57% in 2012. The area proportion of Mild vulnerability has shown a fluctuating upward trend, increasing from 11.92% in 2002 to 18.88% in 2022, with the maximum value of 21.23% occurring in 2017. The area proportions of Moderate and Severe vulnerabilities have not shown significant changes over the 20-year period, with average proportions of 7.64% and 14.58%, respectively. The area proportions of Potential vulnerability peaked at 20.73% in 2012 but remained stable otherwise, with an average proportion of 14.43%.

Spatial characteristics of EV

From the perspective of spatial distribution characteristics (as shown in Fig. 4), the upper, middle, and lower reaches of the LRB exhibit distinct regional heterogeneity, presenting a “low-medium-high” spatial distribution pattern. The upper reaches of the LRB are primarily located in the Inner Mongolian Plateau, where land use types are dominated by grasslands and forests, with a low population density. This area includes parts of Zhangjiakou, Xilinguole, Chifeng, and northern Chengde, and is mainly characterized by Potential vulnerability and Microscopic vulnerability, with Zhangjiakou predominantly exhibiting Mild vulnerability. The middle reaches of the LRB are mainly situated in the Yan Mountain area within Chengde, Chaoyang, and Huludao regions, where the land use type is primarily forested, and the terrain is complex. Human activities are concentrated in valley basin areas, and this region is mainly characterized by Microscopic vulnerability and Mild vulnerability.

Year	Indicators	Principal component						
		PCA1	PCA2	PCA3	PCA4	PCA5	PCA6	PCA7
2002	Eigenvalue	8.423	3.398	1.986	1.539	0.951	0.695	0.569
	contribution rate (%)	44.09	17.78	10.40	8.06	4.98	3.64	2.98
	cumulative contribution rate (%)	44.09	61.87	72.27	80.32	85.30	88.94	91.92
2007	Eigenvalue	9.686	3.798	2.073	1.529	1.019	0.645	0.469
	contribution rate (%)	46.62	18.28	9.98	7.36	4.91	3.10	2.26
	cumulative contribution rate (%)	46.62	64.90	74.88	82.24	87.15	90.25	92.51
2012	Eigenvalue	11.346	3.287	2.228	1.711	1.095	0.633	0.458
	contribution rate (%)	50.76	14.71	9.97	7.65	4.90	2.83	2.05
	cumulative contribution rate (%)	50.76	65.46	75.43	83.09	87.98	90.82	92.87
2017	Eigenvalue	9.990	3.788	2.144	1.604	1.107	0.637	0.442
	contribution rate (%)	47.14	17.87	10.12	7.57	5.22	3.01	2.08
	cumulative contribution rate (%)	47.14	65.01	75.13	82.70	87.92	90.93	93.01
2022	Eigenvalue	10.016	3.527	2.144	1.634	1.083	0.635	0.436
	contribution rate (%)	47.56	16.75	10.18	7.76	5.14	3.02	2.07
	cumulative contribution rate (%)	47.56	64.30	74.48	82.24	87.38	90.40	92.47

Table 4. Results of SPCA.

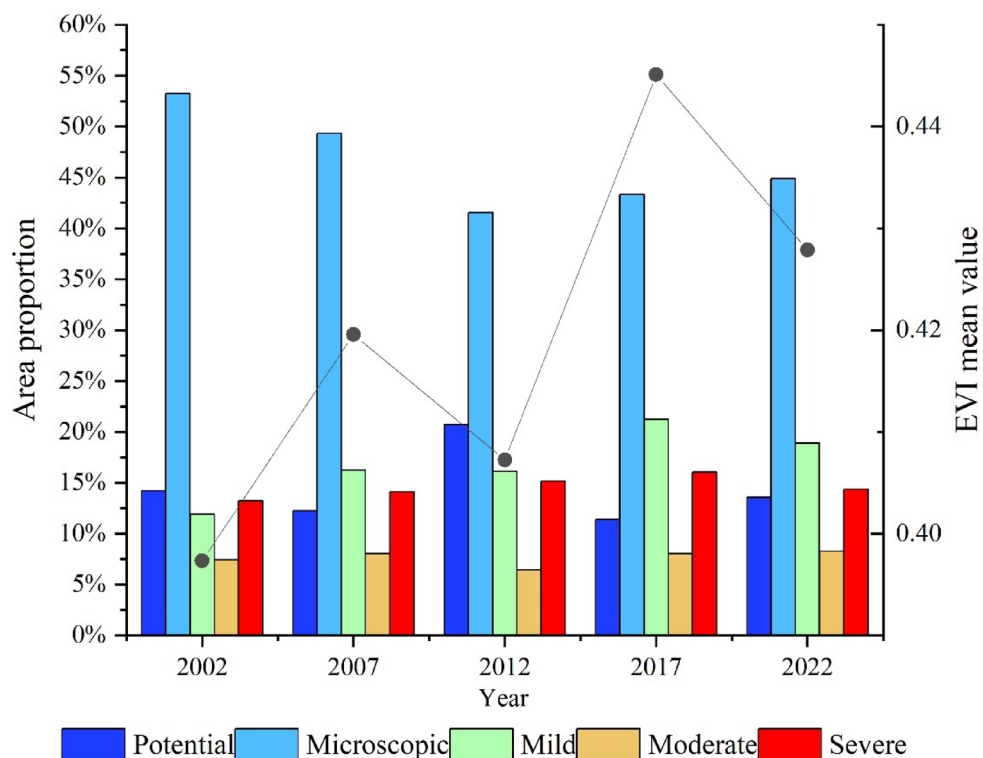


Fig. 3. Temporal changes in area proportions of EV levels in LRB (2002–2022): Shows the percentage distribution of five EV levels (Potential, Microscopic, Mild, Moderate, and Severe vulnerability), with Microscopic vulnerability dominating (average 46.47% coverage).

The lower reaches of the LRB are primarily located in the North China Plain, including areas of Tangshan and Qinhuangdao, where land use types are dominated by construction land and cultivated land. This area is an important industrial base in the BTH region, with a developed economy, and is predominantly characterized by Moderate and Severe vulnerability.

Temporal characteristics of EV

In this study, based on the degree of change in the EV level, the types of change were categorized as Decline, Unchanged, and Increase, as shown in Fig. 5. From the perspective of different periods of change, from 2002

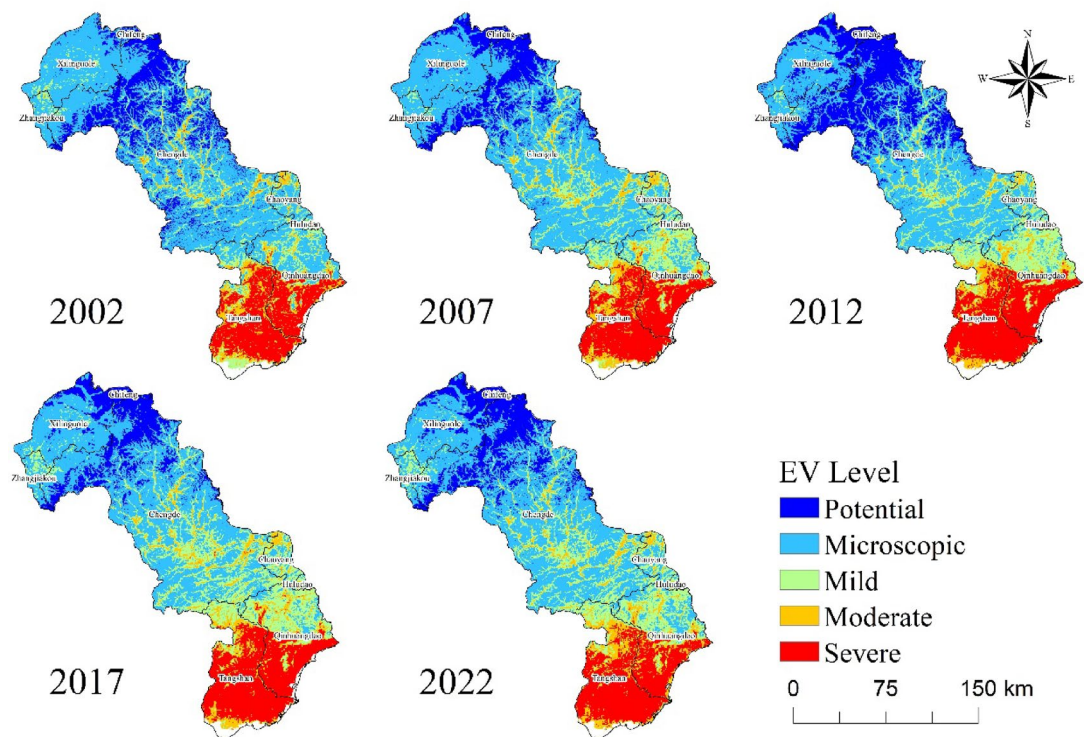


Fig. 4. Spatial distribution patterns of EV levels in LRB (2002–2022): Reveals a distinct “low-medium-high” gradient from northwest (high-altitude areas) to southeast (plains).

to 2007, the areas with a decline in EV level were mainly concentrated in the upper reaches of the LRB—Zhangjiakou, Xilinguole, Chifeng, and northern Chengde, while the rest of the regions showed an upward trend in EV level. From 2007 to 2012, the EV levels in most areas of the upper and middle reaches of the LRB decreased, while in parts of Tangshan, Qinhuangdao, and southern Chengde, the EV levels increased. From 2012 to 2017, the EV levels in the LRB generally increased, with only the southern part of Tangshan and the eastern part of Qinhuangdao experiencing a decline. From 2017 to 2022, the EV levels in the LRB generally decreased, with only the southern part of Tangshan showing an increase.

In this study, to better illustrate the changes in each EV level within the study area, we created a transition Sankey diagram, as shown in Fig. 6. Overall, the inter-level transitions of EV levels were mainly concentrated on transitions between adjacent levels, while transitions across multiple levels accounted for a relatively smaller proportion. From 2002 to 2007, the EV level transition of LRB showed that the largest incoming EV level was Mild vulnerability, with an inflow area of 3688.50 km², an outflow area of 1339.94 km², a net increase of 2348.56 km², a change rate of 36.23%, and the change was mainly distributed in the central and southern parts of Chengde and the northern areas of Qinhuangdao. The largest outgoing EV level was Microscopic vulnerability, with an outflow area of 5012.32 km², an inflow area of 2887.06 km², a net outflow of 2125.17 km², and a change rate of −7.34%, and the change was mainly distributed in Xilinguole, the central and southern parts of Chengde, and the northern areas of Qinhuangdao. The main transition types were “Potential—Microscopic” and “Microscopic—Mild”. From 2007 to 2012, the largest incoming EV level was Potential vulnerability, with an inflow area of 4540.18 km², an outflow area of 36.85 km², a net increase of 4503.33 km², a change rate of 67.60%, and the change was mainly distributed in Xilinguole and the northern parts of Chengde. The largest outgoing EV level was Microscopic vulnerability, with an outflow area of 5599.33 km², an inflow area of 1373.24 km², a net outflow of 4226.09 km², and a change rate of −15.75%, and the change was mainly distributed in the eastern part of Xilinguole, the northern part of Chengde, and the northern part of Qinhuangdao. The main transition types were “Microscopic—Potential” and “Mild—Microscopic”. From 2012 to 2017, the largest incoming EV level was Microscopic vulnerability, with an inflow area of 5118.67 km², an outflow area of 4204.40 km², a net increase of 914.27 km², a change rate of 4.20%, and the change was mainly distributed in the southern part of Xilinguole, and the northern parts of Chengde and Qinhuangdao. Followed by Mild vulnerability, with an inflow area of 4249.77 km², an outflow area of 1465.35 km², a net increase of 2784.42 km², a change rate of 31.77%, and the change was mainly distributed in the southern area of Xilinguole, northern Chengde, and northern Qinhuangdao. The largest outgoing EV level was Potential vulnerability, with an outflow of 4968.45 km², and a change rate of −44.07%, and the change was mainly distributed in the southern part of Xilinguole and the northern part of Chengde. The main transition types were “Potential—Microscopic” and “Microscopic—Mild”. From 2017 to 2022, the largest incoming EV level was Microscopic vulnerability, with an inflow area of 2336.34 km², an outflow area of 1473.01 km², a net increase of 863.33 km², a change rate of 3.66%, and the change was mainly distributed in the southern part of Chengde, the northern part of Qinhuangdao, and the

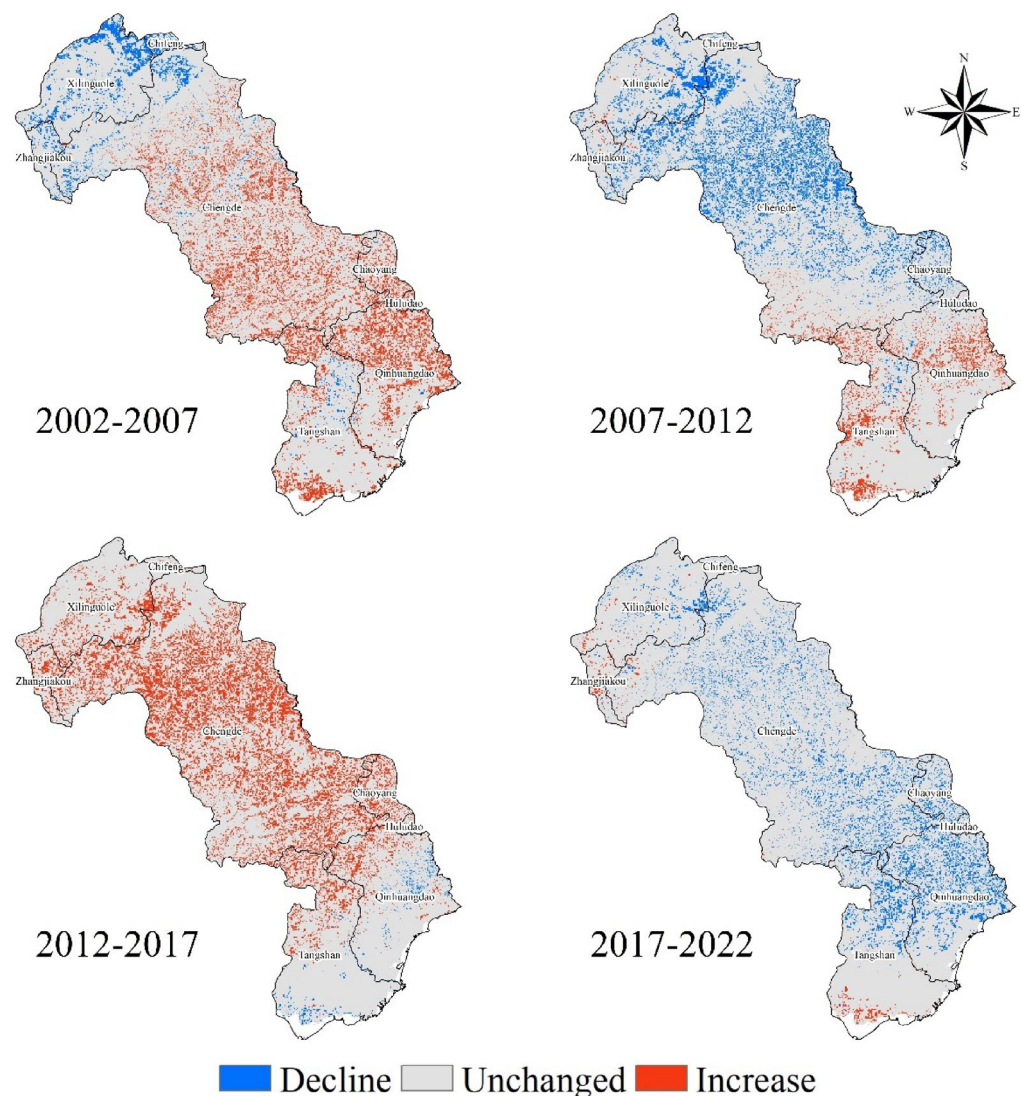


Fig. 5. Spatial patterns of EV level changes: Classifies changes into Decline, Unchanged, and Increase categories, showing different transition patterns across four periods (2002–2007, 2007–2012, 2012–2017, 2017–2022).

northern part of Tangshan. Followed by Potential vulnerability, with an inflow area of 1210.07 km², an outflow area of 20.77 km², a net increase of 1189.30 km², a change rate of 19.21%, and the change was mainly distributed in the southern part of Xilinguole and the northern part of Chengde. The largest outgoing EV level was Mild vulnerability, with an outflow area of 2343.43 km², an inflow area of 1063.12 km², a net outflow of 1280.31 km², and a change rate of −11.09%, and the change was mainly distributed in the northern parts of Tangshan and Qinhuangdao. The main transition types were “Mild—Microscopic”, “Microscopic—Potential”, and “Severe—Moderate”. In the four periods mentioned, the years 2002–2007 and 2012–2017 were primarily characterized by a shift from lower EV levels to higher EV levels, indicating a degree of deterioration in EV. In contrast, the years 2007–2012 and 2017–2022 were marked by a transition from higher EV levels to lower EV levels, suggesting a certain degree of improvement in EV.

The centroid migration model can illustrate the aggregation, dispersion, and migration of EV in the study area spatially. This study analyzed the centroid shift of EV at each level of LRB for each period, obtaining the migration of the centroid positions of EV at each level in the region (as shown in Fig. 7). The results indicated:

- (1) The centroid of Potential vulnerability was mainly located in the northern part of Chengde. From 2002 to 2022, the centroid primarily migrated to the northwest, with an average migration rate of 22.38 km/5-years. The maximum migration speed occurred during the period from 2002 to 2007, reaching 63.49 km.
- (2) The centroid of Microscopic vulnerability was primarily situated in the central part of Chengde. From 2002 to 2017, it mainly migrated to the east and south, and from 2017 to 2022, it began to migrate to the northwest, with an average migration rate of 8.06 km/5-years.

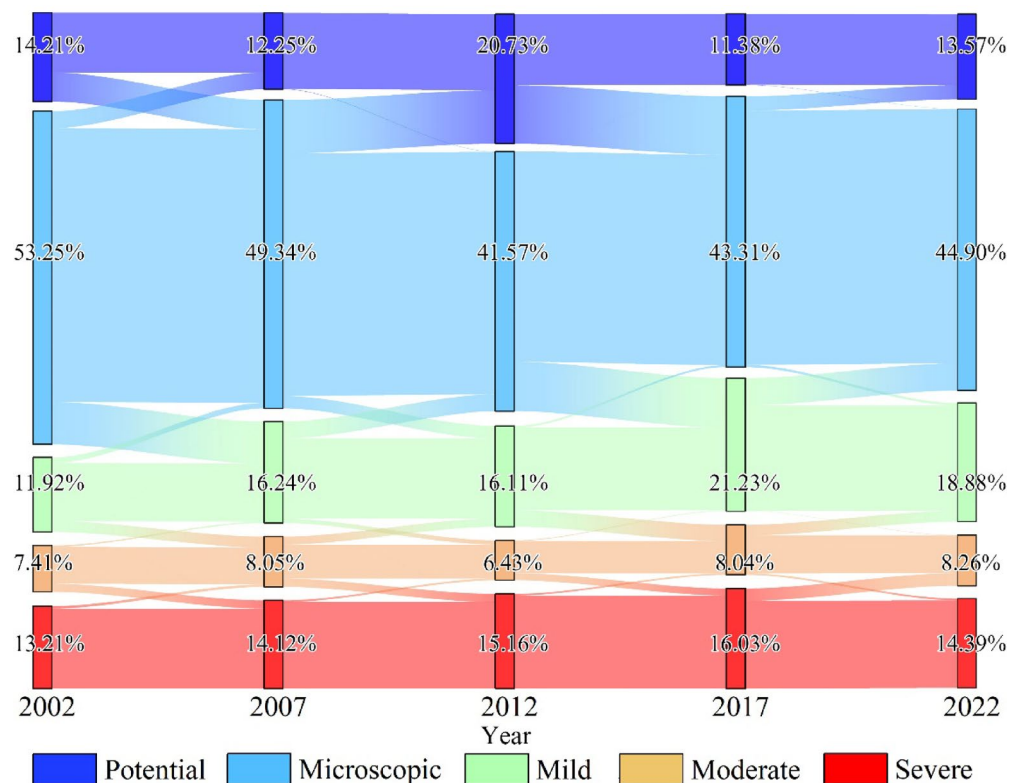


Fig. 6. Sankey diagram of EV level transitions (2002–2022): Visualizes area transfers between 5 EV levels.

- (3) The centroid of Mild vulnerability was mainly distributed in the southern part of Chengde. From 2002 to 2022, the centroid generally migrated to the southeast, with an average migration rate of 11.44 km/5-years.
- (4) The centroid of Moderate vulnerability migrated across the border areas of Chengde, Qinhuangdao, and Tangshan. From 2002 to 2022, the migration directions were “north-southeast-northwest-southeast,” with an average migration rate of 13.62 km/5-years.
- (5) The centroid of Severe vulnerability migrated across the border areas of Tangshan and Qinhuangdao. From 2002 to 2022, the migration directions were “southwest-east-northwest-southeast,” with an average migration rate of 12.06 km/5-years.
- (6) Unlike other EV levels whose centroids mainly shifted over relatively short distances, the Potential vulnerability centroid moved rapidly in a northwest direction (average rate: 22.38 km/5-years). Combined with changes in land-use types, we found that the forest area in Zhangjiakou, Xilinguole, Chifeng and Chengde increased from 13,859.86 km² to 14,137.32 km² (from 2002 to 2022), which might be related to afforestation projects in Chengde and Xilinguole areas (e.g., conversion of cropland to forest in the “Three-North Shelterbelt Program”). Conversely, the southeastward shift of Mild/Moderate/Severe vulnerability centroids was consistent with urban expansion in Tangshan and Qinhuangdao, where the construction land increased from 1615.78 km² to 2659.56 km² (from 2002 to 2022).

Spatial correlation analysis of EV

The Global Moran's I values for the years 2002, 2007, 2012, 2017, and 2022 were 0.889, 0.917, 0.938, 0.931, and 0.922, respectively, indicating a significant clustering phenomenon in the spatial distribution of EV in the LRB region. From 2002 to 2022, the spatial clustering phenomenon of EV in LRB exhibited a trend of increasing initially and then decreasing. Observing the Global Moran's I scatter plot for EV in LRB (Fig. 8), there were significantly fewer points in the second and fourth quadrants compared to the first and third quadrants, suggesting that there were distinct areas with high and low EV in LRB. Furthermore, the number of points in the third quadrant was noticeably less than in the first quadrant, indicating that there were fewer high-high clustering areas of EV than low-low clustering areas in the study area, with the number of high EV clustering areas significantly less than those with low EV.

Figure 9 presented the local autocorrelation LISA cluster maps of EVI in the study area from 2002 to 2022. The spatial aggregation of LRB was mainly characterized by high-high clusters, low-low clusters, and insignificant clusters, with high-low and low-high clusters appearing less frequently and distributed sporadically, accounting for less than 2% of the total area. Among them, the low-low cluster area had the largest proportion, mainly distributed in the regions of Xilinguole, Chifeng, northern Chengde, and southwestern Chengde, where Potential and Microscopic vulnerabilities primarily characterized EV. The average area proportion over the 5 periods reached 46.45%, but overall, it showed a decreasing trend, dropping from 50.83% in 2002 to 44.57% in 2022.

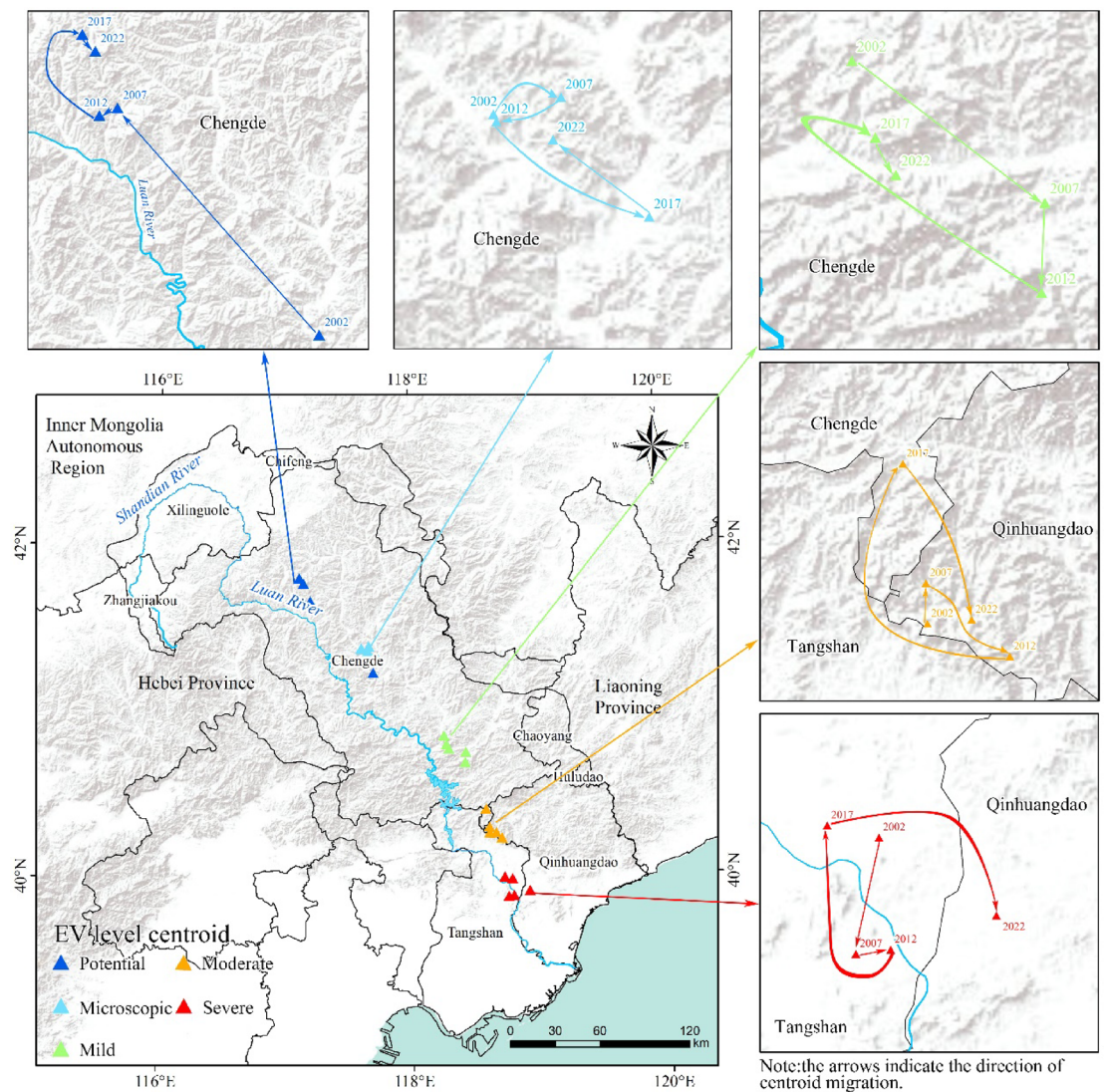


Fig. 7. Centroid migration trajectories of EV levels (2002–2022): Tracks the spatial movement of EV level centroids, showing Potential vulnerability moving northwestward (average 22.38 km/5-years) while other levels generally shifted southeastward.

in 2022, with a significant decrease observed in the southwestern part of Chengde. The high-high cluster areas were mainly distributed in urban areas of Tangshan and the southern part of Qinhuangdao, where EV was mainly characterized by Moderate and Severe vulnerabilities. The average area proportion over the 5 periods was 24.46%, with little overall change, increasing from 22.72% in 2002 to 24.96% in 2022. The insignificant cluster areas were mainly distributed in Zhangjiakou, central Chengde, Chaoyang, Huludao, and the northern part of Qinhuangdao, with an average area proportion of 27.56% over the 5 periods, slightly increasing from 24.04% in 2002 to 28.83% in 2022, indicating that the random spatial distribution characteristics of EV in the study area were strengthening.

Driving factors

Single factor detection analysis

To further explore the driving factors of EVI changes in the study area, this paper used the factor detector in Geodetector to investigate the explanatory power of various factors on EVI. The analysis results were shown in Table 5. (1) The p values of all driving factors were less than 0.001, indicating that each driving factor had significant explanatory power on EVI. (2) There was a certain difference in explanatory power among different years. From 2002 to 2022, the 6 factors that consistently had the strongest influence on the spatial differentiation of EVI in the study area were Elevation (X1), Biological Abundance (X9), Annual average temperature (X5), Cultivated Land Proportion (X15), Annual average precipitation (X4), and Population Density (X17), with q mean values of 0.855, 0.812, 0.800, 0.783, 0.665, and 0.658, respectively, all greater than 0.6, indicating a significant influence and being the dominant driving factors for the spatial differentiation of EVI in the LRB

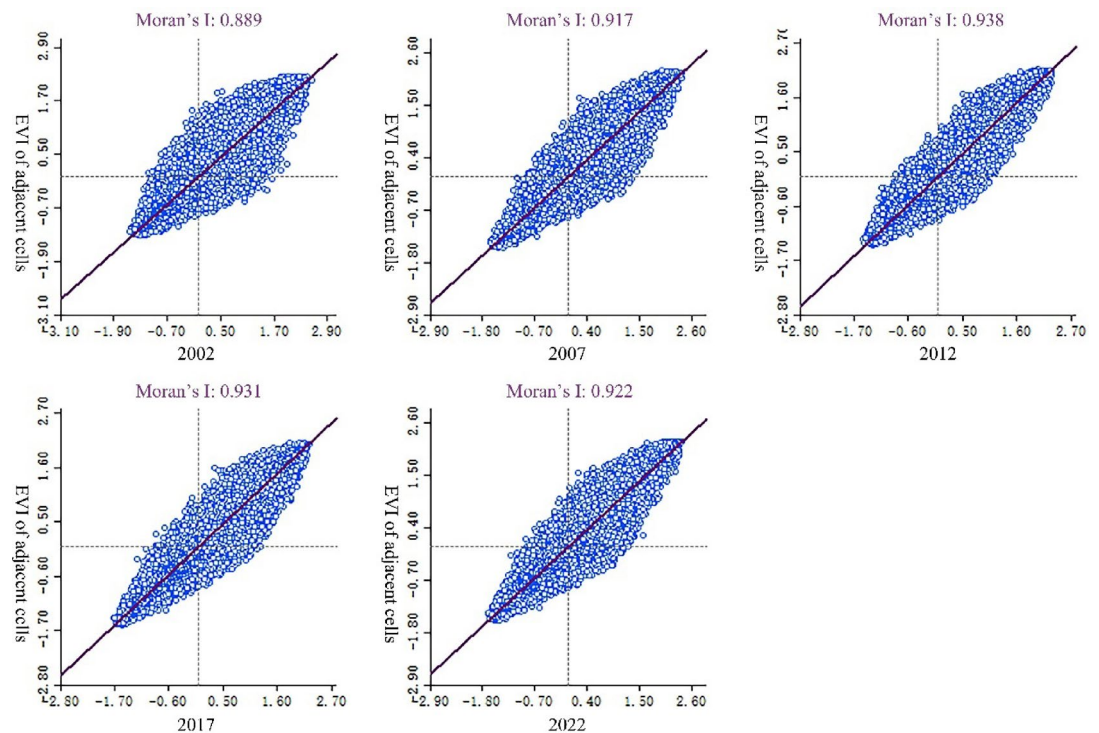


Fig. 8. Global Moran's I scatter plots of EVI (2002–2022): Demonstrates strong spatial autocorrelation (Moran's I: 0.889–0.938, p value < 0.001).

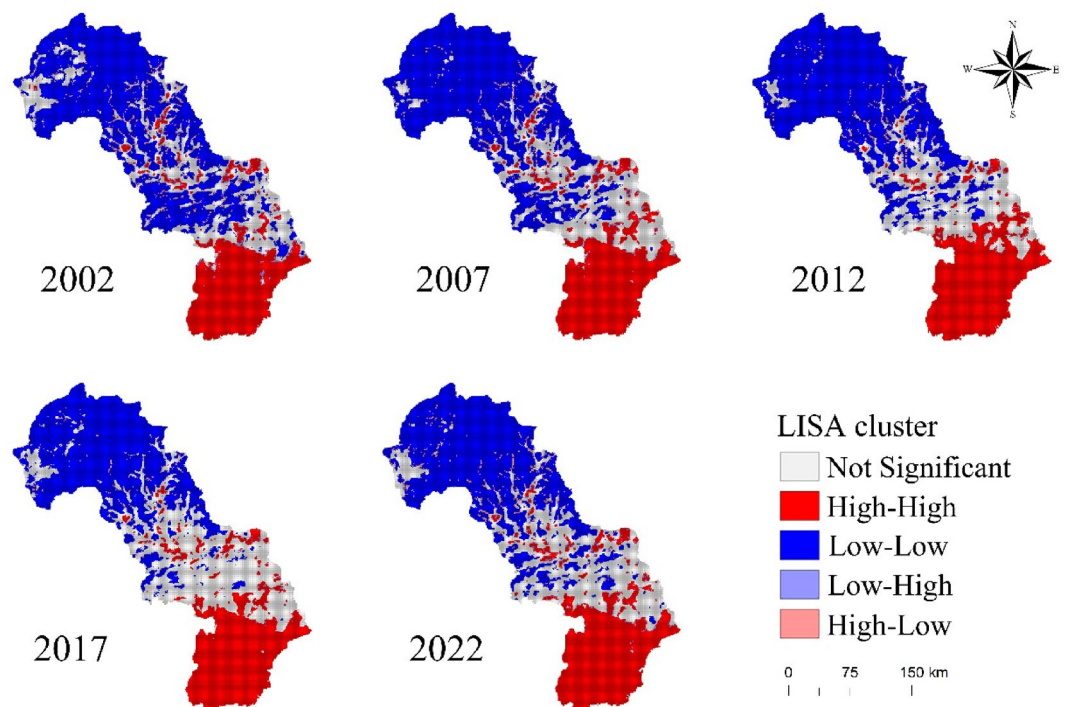


Fig. 9. LISA cluster maps of EVI (2002–2022): Identifies spatial aggregation patterns including high-high clusters (mainly in Tangshan and Qinhuangdao urban areas), low-low clusters (in Xilinguole and northern Chengde), and non-significant clusters.

Factors	2002		2007		2012		2017		2022		2002–2022	
	q value	Rank	q value	Rank	q value	Rank	q value	Rank	q value	Rank	q mean value	Rank
X1	0.794	3	0.856	1	0.893	1	0.869	1	0.863	1	0.855	1
X2	0.382	10	0.304	10	0.297	10	0.272	10	0.297	10	0.310	10
X3	0.393	9	0.312	9	0.305	9	0.278	9	0.305	9	0.319	9
X4	0.453	7	0.674	6	0.760	6	0.723	5	0.713	5	0.665	5
X5	0.732	4	0.791	4	0.835	2	0.817	2	0.827	2	0.800	3
X6	0.245	11	0.261	11	0.250	11	0.266	11	0.264	11	0.257	11
X7	0.436	8	0.476	8	0.787	3	0.579	7	0.561	7	0.568	8
X8	0.168	13	0.136	13	0.081	15	0.075	15	0.052	16	0.103	14
X9	0.896	1	0.822	2	0.782	4	0.774	3	0.786	3	0.812	2
X10	0.091	15	0.082	15	0.086	14	0.087	14	0.087	14	0.086	15
X11	0.140	14	0.135	14	0.131	13	0.126	13	0.132	13	0.133	13
X12	0.014	17	0.024	17	0.032	17	0.051	17	0.043	17	0.033	17
X13	0.078	16	0.066	16	0.071	16	0.059	16	0.065	15	0.068	16
X14	0.203	12	0.185	12	0.179	12	0.188	12	0.188	12	0.189	12
X15	0.890	2	0.811	3	0.742	7	0.733	4	0.738	4	0.783	4
X16	0.543	6	0.592	7	0.565	8	0.590	6	0.585	6	0.575	7
X17	0.669	5	0.742	5	0.765	5	0.561	8	0.553	8	0.658	6

Table 5. The q value of factor detection. The p values of all factors are less than 0.001.

region. (3) Net Primary Productivity (X10), Residential Point Kernel Density (X13), and Shannon Diversity Index (X12) had a smaller impact, with q mean values of 0.086, 0.068, and 0.033, respectively, all less than 0.1.

Interaction detection analysis

This study employed interaction detection to further analyze the impact of interactions between different factors on EVI (as shown in Fig. 10). The results indicated: (1) There was a significant interaction between different driving factors, mainly characterized by two-factor enhancement or nonlinear enhancement. Compared with nonlinear enhancement, two-factor enhancement had a greater explanatory power on the spatial differentiation of EVI in the study area. (2) In 2002, the top 4 interactions in terms of explanatory power were $X1 \cap X9$, $X5 \cap X9$, $X1 \cap X15$, and $X9 \cap X17$, with q-values of 0.965, 0.961, 0.959, and 0.952, respectively. In 2007, the top 4 interactions were $X1 \cap X9$, $X1 \cap X15$, $X5 \cap X9$, and $X7 \cap X9$, with q-values of 0.970, 0.966, 0.964, and 0.961, respectively. In 2012, the top 4 interactions were $X7 \cap X9$, $X1 \cap X9$, $X1 \cap X15$, and $X4 \cap X9$, with q-values of 0.969, 0.967, 0.964, and 0.960, respectively. In 2017, the top 4 interactions were $X1 \cap X9$, $X5 \cap X9$, $X1 \cap X15$, and $X7 \cap X9$, with q-values of 0.970, 0.966, 0.964, and 0.963, respectively. In 2022, the top 4 interactions were $X1 \cap X9$, $X5 \cap X9$, $X1 \cap X15$, and $X7 \cap X9$, with q-values of 0.966, 0.964, 0.962, and 0.959, respectively. (3) From 2002 to 2022, the interactions between X1, X5, X9, X15, and other factors had q-values above 0.70, with an explanatory degree greater than 70%, significantly stronger than the interactions between other factors. (4) The interactions between X12 and other elements often showed nonlinear growth, indicating a more complex interactive relationship with other factors and enhancing its ultimate explanatory power.

Overall, the interactions between multiple factors had a significant enhancing effect on the spatial differentiation characteristics of EVI, indicating that the spatial differentiation characteristics of EVI in the study area are formed by the interaction of multiple factors. Among them, Elevation (X1), Annual average temperature (X5), Biological Abundance (X9), and Cultivated Land Proportion (X15) have shown stronger explanatory power than other factors in both factor detection and interaction detection, being the main driving factors of EVI in the LRB region and leading to the spatial distribution differences of EVI. Therefore, when protecting and managing the ecological environment of the region, the impact of the aforementioned driving factors on EV should be fully considered.

Driving mechanisms

The spatial distribution of primary driving factors (Fig. 11) suggested their key roles in influencing the LRB’s EV gradient, though interactions were complex:

Elevation (X1) served as a foundational control, with high-altitude areas (e.g., Northwest Xilinguole/Zhangjiakou; > 1300 m) generally supporting more intact ecosystems but exhibiting increased erosion susceptibility on steeper slopes. Low-elevation plains (Southeast Tangshan/Qinhuangdao; < 500 m) experienced intensified human pressure. Biological Abundance (X9) tended to peak in forested Northwest (mountains), likely enhancing soil and hydrological stability, while declining markedly in Southeast lowlands where cultivated land expansion ($X15 > 66\%$) may drive habitat simplification and soil degradation. Annual Temperature (X5) showed a complementary pattern: Warmer Southeast conditions could exacerbate moisture stress and nutrient cycling rates, potentially reducing resilience, whereas cooler Northwest temperatures may slow ecosystem recovery. The co-occurrence of low X1, high X15, low X9, and high X5 in the Southeast plains aligns spatially with the observed EV hotspot, implying that anthropogenic pressures may override natural advantages in these areas. Conversely,

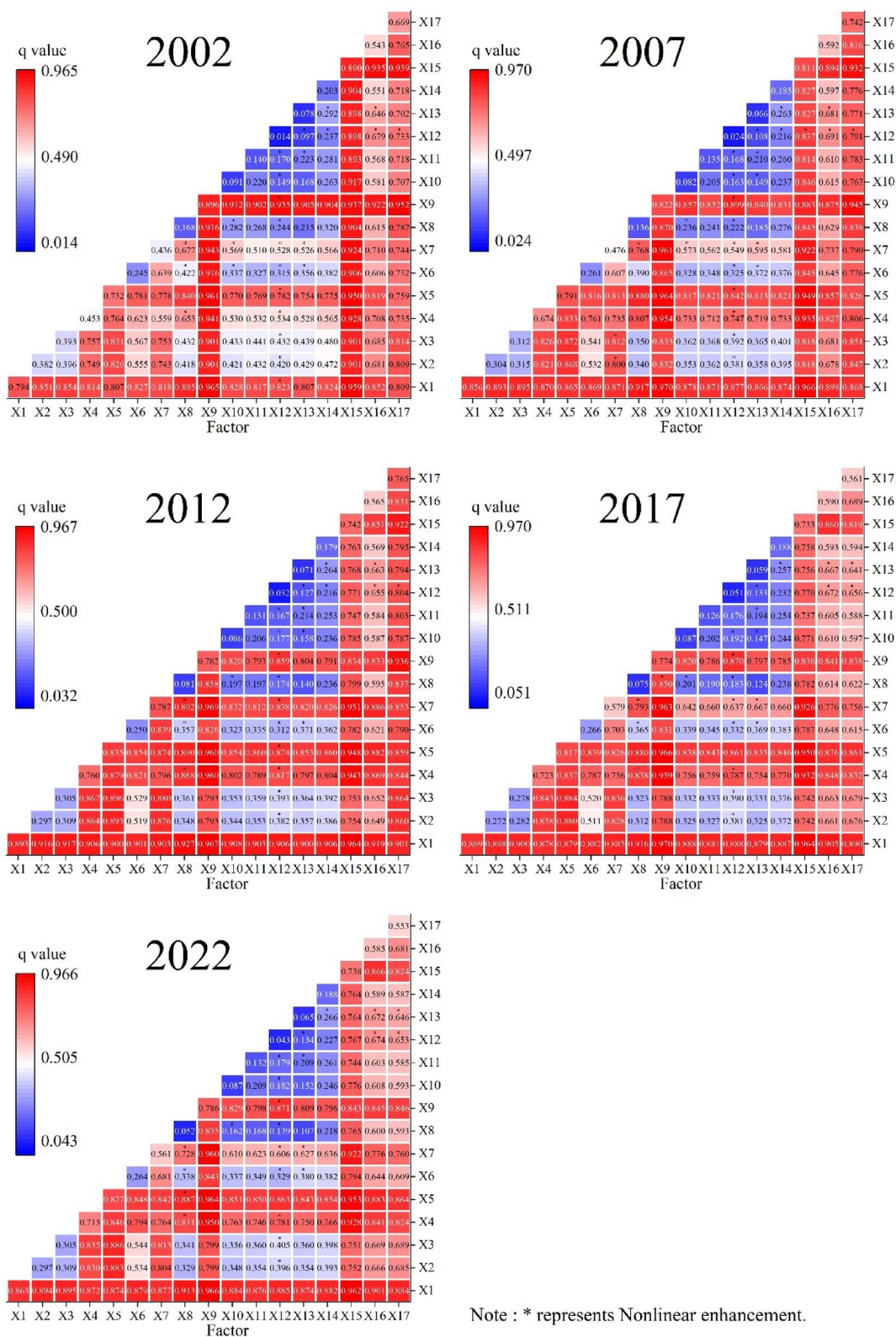


Fig. 10. Interaction detection results of driving factors (2002–2022): Analyzes pairwise interactions between 17 factors, showing X1, X5, X9 and X15 having the strongest interactive effects.

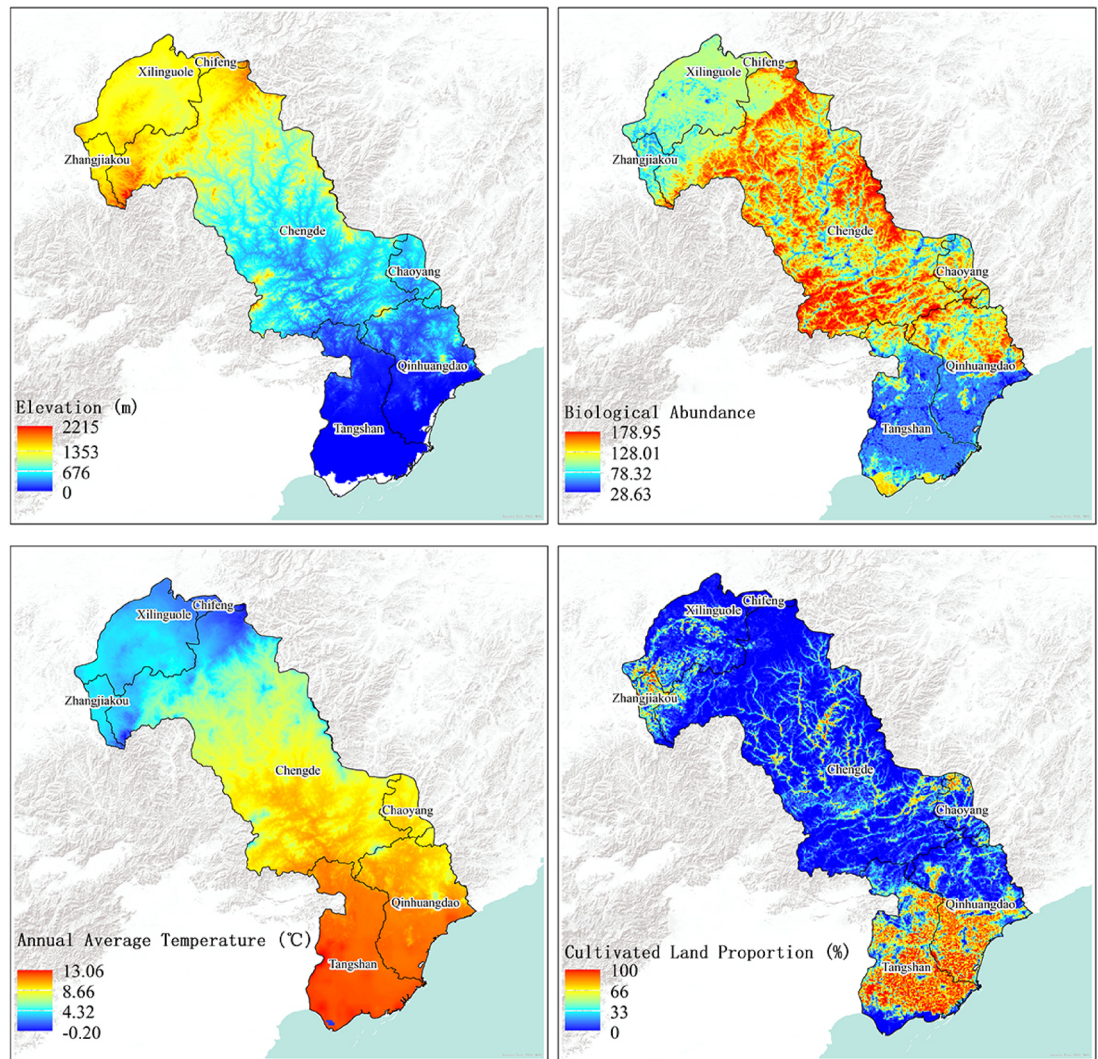


Fig. 11. Spatial distribution of primary driving factors: Maps the four most influential driving factors.

the Northwest's high X1, low X15, high X9, and low X5 correlated with lower EVI. This spatial synergy highlights how elevation-mediated processes interact with human land use to shape vulnerability patterns.

Forecast

In this study, we drew on the research of Ru et al.⁴⁹ and selected an iteration coefficient of 10, a 5×5 filter, and a proportional error of 0.15 to calculate the probability transition matrix using data from 2002 and 2012. The CA-Markov module in IDRISI Selva 17 was utilized for forecasting EV for the year 2022, and the CROSSTAB tool was employed for the calculation of Kappa coefficients and precision testing⁵⁰. The calculated Kappa coefficient for the actual and simulated EV values of LRB in 2022 is 0.8603, with a p value less than 0.001, indicating high accuracy of the forecasting model and reliable results, making it suitable for forecasting and simulating EV in the LRB area for the year 2032. Figure 12 presented the results of our forecast of EV in the study area for 2032, based on data from 2012 and 2022. Overall, the area proportions of Potential vulnerability, Microscopic vulnerability and Severe vulnerability decreased by 5.83%, 2.01% and 2.30%, respectively, while those of Mild vulnerability and Moderate vulnerability increased by 6.57% and 3.57%, respectively. There was a trend of reduction in Potential vulnerability in the upstream areas of LRB by 2032, while Mild and Moderate vulnerabilities showed spatial expansion trends in the midstream and downstream areas of LRB. Specifically: (1) In the upstream areas of LRB, there was a noticeable decrease in Potential vulnerability in the northern part of Chengde, and an expansion trend of Mild vulnerability in the Zhangjiakou area. (2) In the midstream areas of LRB, including central Chengde, Chaoyang, Huludao, and the northern part of Qinhuangdao, Mild and Moderate vulnerabilities were expanding into surrounding regions. (3) In the downstream areas of LRB, Moderate vulnerability in Tangshan and Qinhuangdao areas was spreading towards the southern regions, while Severe vulnerability was contracting towards the central urban areas.

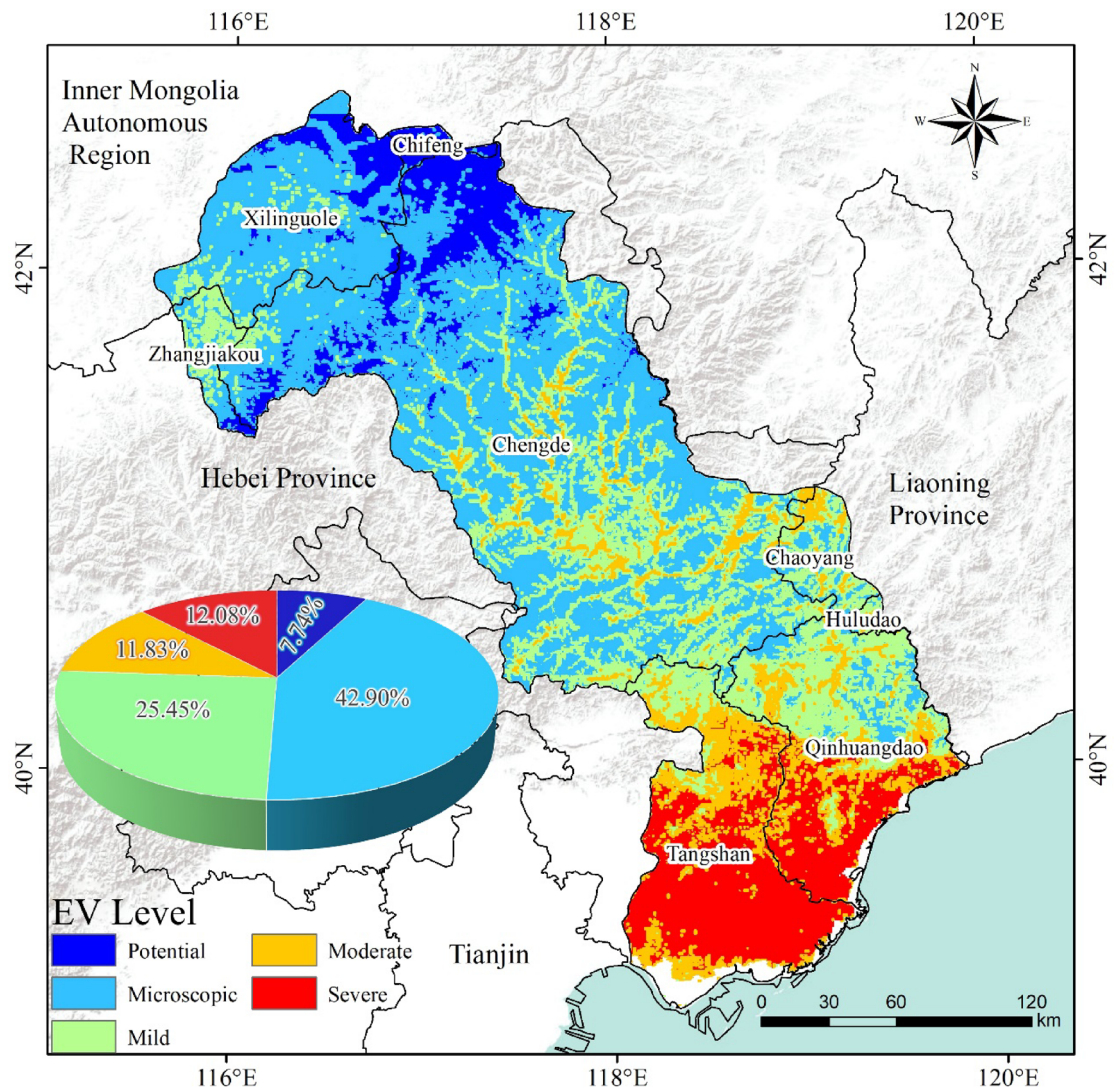


Fig. 12. CA-Markov forecast of EV levels for 2032: Projects decreases in Potential (−5.83%), Microscopic (−2.01%) and Severe (−2.30%) vulnerability areas, with increases in Mild (+6.57%) and Moderate (+3.57%) vulnerability areas compared to 2022 levels.

Discussion

Distribution Pattern of EV in LRB

This study, based on the SRP model, selected 17 indicators to construct an EV evaluation index system and evaluated the EV of the LRB from 2002 to 2022. In terms of the spatial distribution pattern of EV, a “low–medium–high” gradient from northwest to southeast is observed across the upper, middle, and lower reaches of the LRB, with a distinct spatial clustering characteristic. The areas with higher EV in the LRB are concentrated in the downstream regions of Qinhuangdao and Tangshan, which are important industrial bases in the BTH region. These areas have low vegetation coverage, high landscape fragmentation, high population density, and land use types are relatively singular, dominated by cultivated land and construction land, leading to high EV. In contrast, areas far from urban centers, such as mountainous or plateau regions, exhibit lower EV. For instance, the Yanshan Mountain Range in the middle and upper reaches of the LRB and the Inner Mongolia Plateau, characterized by high vegetation coverage, complex landscape structure, low landscape fragmentation, and diverse ecological functions, have lower EV. Particularly in areas dominated by forest land, such as northern Chengde and Chifeng, the EV is mainly Potential vulnerability, which may be related to China's largest afforestation project since 1978—the Three-North Shelter Forest Program (the LRB is the most afforested watershed in North China and an important part of the Three-North Shelter Forest Program)²¹.

From a temporal perspective, the EVI of the LRB region has shown an overall fluctuating upward trend over the 20 years. The area proportion of Potential and Microscopic vulnerability has decreased, while the area proportions of Mild, Moderate, and Severe vulnerability have all increased. In terms of centroid migration, the spatial trajectories reveal significant reconfiguration of ecological pressures. The northwestward shift of the Potential vulnerability centroid corresponds to China's ecological restoration policies (e.g., the ‘Grain for

Green' Project), which reduced human disturbance in high-altitude regions through afforestation and grazing restrictions. Conversely, the predominant southeastward migration of other EV-level centroids (particularly Mild, Moderate, and Severe vulnerability) aligns with the expansion of high-vulnerability areas in the middle-lower basin. This pattern correlates strongly with coastal industrialization (e.g., land reclamation at Tangshan Port) and accelerated economic development following China's 2001 WTO accession, which triggered rapid urban expansion and intensified human activities. These opposing trajectories—conservation-driven northwest migration versus development-driven southeast shifts—effectively capture the regional trade-offs between ecological protection and economic growth, with the latter exerting significant pressure on downstream ecosystems through construction land proliferation⁵¹.

A comparison with existing research in China shows that many rivers follow a common pattern: EV levels are lower in western upstream areas and higher in eastern downstream ones. Studies like Ru et al.'s on the Yellow River Basin and Pan et al.'s on the Yangtze River Basin have noted this pattern^{49,52}. This may stem from China's west—high—east—low topography and the rapid urbanization in eastern plains. Notably, the LRB has a higher spatial clustering degree. Most Moderate and Severe vulnerabilities are in the downstream North China Plain. Also, over time, additional Moderate and Severe vulnerabilities mainly emerge in these low-elevation areas. The driving factor analysis shows that topographic factors (elevation) most strongly explain the spatial EV differences, followed by climatic factors and human activities. This differs from some other studies. For example, Wu et al.'s research on the Dongjiang Basin indicates that climatic factors have the strongest explanatory power⁵³. This finding reveals a unique driving mechanism in the LRB, offering a basis for region-specific ecological restoration policies there.

Simulation and forecast of EV in LRB

This study, based on the CA–Markov model, utilized the EV evaluation results from 2002, 2012, and 2022 to forecast the distribution pattern of EV in the LRB for the year 2032. The outcomes were found to be in line with the spatial distribution pattern of EV in the LRB over the past two decades. By comparing the forecasted results for 2022 with the actual evaluation results for the same year, a Kappa coefficient of 0.8603 was obtained, indicating that the forecasted outcomes meet future requirements. Upon comparing the forecasted results for 2032 with the evaluation results from 2022, it was observed that the area proportions of Potential and Microscopic vulnerabilities further decreased, while the area proportions of Mild and Moderate vulnerabilities increased. Geographically, this was primarily characterized by the spread of Mild and Moderate vulnerability from the regions of Zhangjiakou, Chengde, Chaoyang, and Huludao to their surroundings. This reflects an anticipated increase in EV and environmental degradation in the study area by 2032, likely due to the growing demand for land from urban spaces as a result of socio-economic development, leading to urban expansion and the consequent deterioration of the original ecological environment surrounding cities. Concurrently, there was a noted decrease in the area proportion of Severe vulnerability, particularly evident in the southern urban suburbs of Tangshan and Qinhuangdao, where the EV level shifted from Severe vulnerability to Moderate vulnerability. This may be attributed to the ongoing series of ecological restoration projects in these areas^{54,55}.

Policy recommendations

As a critical ecological barrier and water source for the BTH region, LRB's conservation is pivotal for regional sustainability. The EV in the upper, middle, and lower reaches of the LRB exhibit different temporal evolution trends and spatial distribution characteristics. Therefore, each region must develop governance and protection measures that are suitable for its natural conditions and in line with the overall development needs. It is essential to prevent excessive human interference that could further exacerbate EV, while also strengthening ecological protection to enhance the resilience of the ecological environment.

This study, with the aid of Geodetector, unveiled the driving mechanisms behind the EV in the LRB. It was found that Elevation, Annual average temperature, Biological Abundance, and Cultivated Land Proportion are the most significant driving factors, indicating that the spatiotemporal distribution differences in EV are the result of a combination of various natural conditions and human activities. Among human activities, Cultivated Land Proportion, which represents agricultural activities, has the strongest explanatory power. Therefore, moderately restricting the expansion of cultivated land in the LRB basin will have a positive impact on improving the ecological environment. Additionally, Biological Abundance, with its explanatory power second only to Elevation, can serve as an important reference indicator for policy-making.

Based on the findings, we recommend the following:

- (1) The upper and middle reaches of the LRB have relatively lower levels of EV, primarily characterized by Potential, Microscopic, and Mild vulnerabilities. These EV levels are mainly due to natural features such as high elevation, high vegetation coverage, and complex terrain. However, with the continuous expansion of human agricultural activities, the impact on the ecological environment is becoming increasingly intense, leading to an expansion in the area of Mild and Moderate vulnerabilities in the upper reaches. For instance, the Mild vulnerability in the Zhangjiakou area is mainly distributed in the range of cultivated land. Therefore, future ecological protection efforts should be implemented in three phases: Short-term (1–3 years): Prioritize ecological restoration efforts in Zhangjiakou and Xilinguole, where the cultivated land proportion ($q=0.783$) is the main human-driven factor. Restrict the annual expansion of cultivated land in areas with an $EVI > 0.4$ (the mild vulnerability threshold). Launch pilot projects for natural grassland restoration, with the goal of reducing the local EVI. Medium-term (3–5 years): Phasing out intensive grazing in high-elevation sensitive areas such as Xilinguole and Chifeng, implementing rotational grazing, reducing livestock density, and expanding the planting of native tree species along river corridors will help increase biological abundance ($q=0.812$, one of the dominant driving factors) and mitigate the regional EV. Long-term

- (5+ years): Combine water conservation with ongoing afforestation. Through collaborative cross-regional governance, focus on restoring hydrological connectivity and biodiversity corridors.
- (2) The lower reaches of the LRB are the most economically developed areas with substantial human economic activity intervention and high land development, resulting in Moderate and Severe vulnerabilities being predominant in the downstream ecological environment. Therefore, a tiered approach is recommended for future urban planning in cities within the lower reaches of the LRB. Immediate actions (1–2 years): All new urban development plans should reserve ecological space (e.g., parks, wetlands) and enhance green-space connectivity in cities like Tangshan and Qinhuangdao. This may reduce the interactive impact of annual average temperature (X5) and biological abundance (X9) on EVI (the q -value of interaction detection was 0.964 in 2022, the second highest among all factor pairs). Mid-term strategy (2–4 years): Relocate scattered industrial sites from low-elevation ecologically sensitive areas. Implement comprehensive rural land consolidation, restoring degraded land via soil remediation and riparian buffer creation. Long-term strategy (ongoing): Enforce strict industrial—mining land—use auditing to prevent urban sprawl into suburban ecological buffers. Promote agroecological practices in peri-urban farmlands to balance economic output with ecosystem resilience.

Limitations and future perspectives

This study, relying on the SRP model, established an EV evaluation index system for the LRB, calculated the EVI from 2002 to 2022, and analyzed the spatiotemporal distribution pattern and spatial correlation of EV, explored its driving mechanisms, and forecasted the future spatial distribution pattern of EV. However, there are some limitations and uncertainties in the research process: (1) The comprehensive and objective selection of evaluation indicators is a common challenge faced in EV evaluation, with numerous influencing factors (such as extreme weather, geological disasters, policy factors, etc.). However, due to limitations in data availability, spatial resolution, and the difficulty in quantifying some data, not all indicators affecting EV were included in this study. The impact of these indicators on EV needs further analysis in future research. (2) The simulation remains constrained by several limitations. Due to data availability, the 1×1 km spatial resolution—while adequate for basin-scale analyses—may mask localized EV hotspots. The CA-Markov transition rules are derived from historical probabilities and therefore may inadequately account for future socioeconomic shocks or policy interventions, and the neighborhood effect can oversimplify ecological processes that involve long-distance interactions. Moreover, the absence of explicit scenario design implies that the model merely extrapolates EV dynamics under a “business-as-usual” trajectory. Consequently, improving the simulation accuracy of regional EV will be a key focus of our future research. (3) The Geodetector can only judge the explanatory power from the similarity of spatial distribution, and there is a lack of in-depth explanation of the underlying influencing mechanisms, which still requires further experimentation and verification.

Conclusions

This study constructed an evaluation index system using 17 natural and anthropogenic indicators based on the SRP model, and applied SPCA to calculate the EVI for the LRB from 2002 to 2022. Combined with spatial correlation analysis, Geodetector, and CA-Markov model, we systematically analyzed the spatiotemporal dynamics, driving mechanisms, and future trends of EV in the basin.

The key finding showed that the EVI in the LRB presented a fluctuating upward trend over the 20 years (ranging from 0.397 to 0.428), with spatial distribution characterized by a “low-medium-high” gradient from northwest to southeast and significant clustering (Global Moran's I : 0.889–0.938). Geodetector identified elevation ($q=0.855$), biological abundance ($q=0.812$), annual average temperature ($q=0.800$), and cultivated land proportion ($q=0.783$) as the dominant driving factors, with interactions between factors exerting stronger explanatory power on EV. CA-Markov forecasts indicated that by 2032, Potential, Microscopic, and Severe vulnerability areas would decrease, while Mild and Moderate vulnerability areas would expand.

This study provides a scientific basis for targeted ecological protection and management in the LRB by quantifying long-term EV dynamics and revealing key driving mechanisms, contributing to balanced regional ecological conservation and sustainable development.

Data availability

All data generated or analysed during this study are included in this published article.

Received: 4 March 2025; Accepted: 2 September 2025

Published online: 26 September 2025

References

- He, S., Nong, L., Wang, J., Zhong, X. & Ma, J. Revealing various change characteristics and drivers of ecological vulnerability in the mountains of southwest China. *Ecol. Ind.* **167**, 112680. <https://doi.org/10.1016/j.ecolind.2024.112680> (2024).
- Ippolito, A., Sala, S., Faber, J. H. & Vigli, M. Ecological vulnerability analysis: A river basin case study. *Sci. Total Environ.* **408**, 3880–3890. <https://doi.org/10.1016/j.scitotenv.2009.10.002> (2010).
- Folke, C. Resilience: The emergence of a perspective for social–ecological systems analyses. *Glob. Environ. Chang.* **16**, 253–267. <https://doi.org/10.1016/j.gloenvcha.2006.04.002> (2006).
- Adger, W. N., Brooks, N., Bentham, G., Agnew, M. . *New indicators of vulnerability and adaptive capacity*, <<https://www.tyndall.ac.uk/>> (2004).
- Niu, W. Y. The discriminatory index with regard to the weakness, overlapness, and breadth of ecotone. *Acta Ecol. Sin.* **9**(2), 97–105 (1989).
- IPCC. In *Climate Change 2022: Mitigation of Climate Change* (Cambridge University Press, Cambridge, 2022).

7. Hong, W. et al. Establishing an ecological vulnerability assessment indicator system for spatial recognition and management of ecologically vulnerable areas in highly urbanized regions: A case study of Shenzhen China. *Ecol. Indic.* **69**, 540–547. <https://doi.org/10.1016/j.ecolind.2016.05.028> (2016).
8. Hu, X., Ma, C., Huang, P. & Guo, X. Ecological vulnerability assessment based on AHP-PSR method and analysis of its single parameter sensitivity and spatial autocorrelation for ecological protection—A case of Weifang City China. *Ecol. Indic.* **125**, 107464. <https://doi.org/10.1016/j.ecolind.2021.107464> (2021).
9. Zou, T. & Yoshino, K. Environmental vulnerability evaluation using a spatial principal components approach in the Daxing'anling region China. *Ecol. Indic.* **78**, 405–415. <https://doi.org/10.1016/j.ecolind.2017.03.039> (2017).
10. Jiang, B. et al. Change of the spatial and temporal pattern of ecological vulnerability: A case study on Cheng-Yu urban agglomeration. *Southwest China. Ecol. Indic.* **149**, 110161. <https://doi.org/10.1016/j.ecolind.2023.110161> (2023).
11. Prato, T. Decision errors in evaluating tipping points for ecosystem resilience. *Ecol. Ind.* **76**, 275–280. <https://doi.org/10.1016/j.ecolind.2017.01.013> (2017).
12. Qiao, Q., Gao, J., Wang, W., Tian, M. & Lv, S. Method and application of ecological fragility assessment. *Res. Environ. Sci.* **21**(5), 117–123 (2008).
13. He, L., Shen, J. & Zhang, Y. Ecological vulnerability assessment for ecological conservation and environmental management. *J. Environ. Manag.* **206**, 1115–1125. <https://doi.org/10.1016/j.jenvman.2017.11.059> (2018).
14. Zou, T., Chang, Y., Chen, P. & Liu, J. Spatial-temporal variations of ecological vulnerability in Jilin Province (China), 2000 to 2018. *Ecol. Ind.* **133**, 108429. <https://doi.org/10.1016/j.ecolind.2021.108429> (2021).
15. Li, D., Huan, C., Yang, J. & Gu, H. Temporal and spatial distribution changes, driving force analysis and simulation prediction of ecological vulnerability in Liaoning Province China. *Land* **11**, 1025. <https://doi.org/10.3390/land11071025> (2022).
16. Zhang, X. et al. Spatiotemporal evolution of ecological vulnerability in the Yellow River Basin under ecological restoration initiatives. *Ecol. Ind.* **135**, 108586. <https://doi.org/10.1016/j.ecolind.2022.108586> (2022).
17. Yang, N., Zhang, T., Li, J., Feng, P. & Yang, N. Landscape ecological risk assessment and driving factors analysis based on optimal spatial scales in Luan River Basin China. *Ecol. Ind.* **169**, 112821. <https://doi.org/10.1016/j.ecolind.2024.112821> (2024).
18. Liu, J. et al. Ecological risk of heavy metals in sediments of the Luan River source water. *Ecotoxicology* **18**, 748–758. <https://doi.org/10.1007/s10646-009-0345-y> (2009).
19. Wu, Y., Zhang, X., Fu, Y., Hao, F. & Yin, G. Response of vegetation to changes in temperature and precipitation at a semi-arid area of Northern China based on multi-statistical methods. *Forests* **11**, 340. <https://doi.org/10.3390/f11030340> (2020).
20. Zhao, J. et al. Large-scale flood risk assessment under different development strategies: The Luanhe River Basin in China. *Sustain. Sci.* **17**, 1365–1384. <https://doi.org/10.1007/s11625-021-01034-6> (2022).
21. Xu, J., Barrett, B. W. & Renaud, F. G. Ecosystem services and disservices in the Luanhe River Basin in China under past, current and future land uses: Implications for the sustainable development goals. *Sustain. Sci.* **17**, 1347–1364. <https://doi.org/10.1007/s11625-021-01078-8> (2022).
22. Bao, K., Liu, J.-L., You, X.-G., Shi, X. & Meng, B. A new comprehensive ecological risk index for risk assessment on Luanhe River China. *Environ. Geochem. Health* **40**, 1965–1978. <https://doi.org/10.1007/s10653-017-9978-6> (2018).
23. Yue, S. et al. Quantitative evaluation of the impact of vegetation restoration and climate variation on runoff attenuation in the Luan River Basin based on the extended Budyko model. *Land* **12**, 1626. <https://doi.org/10.3390/land12081626> (2023).
24. Wang, Q. et al. Surface water resource attenuation attribution and patterns in Hai River Basin, China. *China Earth Sci.* **67**, 1545–1560. <https://doi.org/10.1007/s11430-023-1268-4> (2024).
25. NASA. (NASA EOSDIS Land Processes DAAC, 2018). <https://doi.org/10.5067/ASTER/ASTGTM.003>
26. GISRS. (ed GISRS) (Geographic remote sensing ecological network platform, 2024). <http://www.gisrs.cn>
27. Running, S., Mu, Q., Zhao, M. (NASA EOSDIS Land Processes Distributed Active Archive Center, 2024). <https://doi.org/10.5067/MODIS/MOD17A3HGF061>
28. Wieder, W. (ORNL Distributed Active Archive Center, 2014). <https://doi.org/10.3334/ORNLDAAAC/1247>
29. Shouzhang, P. (ed Center National Tibetan Plateau Data) (National Tibetan Plateau Data Center, 2024). <https://doi.org/10.11888/Meteor.tpdc.270961>
30. Shouzhang, P. (ed Center National Tibetan Plateau Data) (National Tibetan Plateau Data Center, 2024). <https://doi.org/10.5281/zenodo.3114194>
31. Zhang, X. et al. GLC_FCS30: Global land-cover product with fine classification system at 30 m using time-series Landsat imagery. *Earth Syst. Sci. Data* **13**, 2753–2776. <https://doi.org/10.5194/essd-13-2753-2021> (2021).
32. NGCC. (ed NGCC) (National Geomatics Center of China, 2019) <<http://www.ngcc.cn/>>.
33. Sims, K. et al. *LandScan Global* (Oak Ridge National Laboratory, 2023). <https://doi.org/10.48690/1529167>
34. Zhang, W., Xie, Y. & Liu, B. Estimation of rainfall erosivity using rainfall amount and rainfall intensity. *Geogr. Res.* **21**, 384–390. <https://doi.org/10.11821/yj2002030014> (2002).
35. Williams, J. R. The erosion-productivity impact calculator (EPIC) model: A case history. *Philos. Trans. R. Soc. London Ser. B Biol. Sci.* **329**, 421–428. <https://doi.org/10.1098/rstb.1990.0184> (1990).
36. MEE. (Ministry of Ecology and Environment of the People's Republic of China 2015), <<https://www.mee.gov.cn/ywgz/fgbz/bz/bzwb/stzl/201503/W020150326489785523925.pdf>>.
37. Xu, C. et al. Spatiotemporal variations of eco-environmental vulnerability in Shiyang River Basin China. *Ecol. Indic.* **158**, 111327. <https://doi.org/10.1016/j.ecolind.2023.111327> (2024).
38. Kang, H. et al. A feasible method for the division of ecological vulnerability and its driving forces in Southern Shaanxi. *J. Clean. Prod.* **205**, 619–628. <https://doi.org/10.1016/j.jclepro.2018.09.109> (2018).
39. Chen, X., Li, X., Eladawy, A., Yu, T. & Sha, J. A multi-dimensional vulnerability assessment of Pingtan Island (China) and Nile Delta (Egypt) using ecological sensitivity-resilience-pressure (SRP) model. *Hum. Ecol. Risk Assess. Int. J.* **27**, 1860–1882. <https://doi.org/10.1080/10807039.2021.1912585> (2021).
40. Chen, K., Dong, Z. & Gong, J. Monitoring dynamic mangrove landscape patterns in China: Effects of natural and anthropogenic forcings during 1985–2020. *Eco. Inform.* **81**, 102582. <https://doi.org/10.1016/j.ecoinf.2024.102582> (2024).
41. Kumari, M., Sarma, K. & Sharma, R. Using Moran's I and GIS to study the spatial pattern of land surface temperature in relation to land use/cover around a thermal power plant in Singrauli district, Madhya Pradesh, India. *Remote Sens. Appl. Soc. Environ.* **15**, 100239. <https://doi.org/10.1016/j.rsase.2019.100239> (2019).
42. Jing, Y., Zhang, F., He, Y., Johnson, V. C. & Arikana, M. Assessment of spatial and temporal variation of ecological environment quality in Ebinur Lake Wetland national nature reserve, Xinjiang China. *Ecol. Indic.* **110**, 105874. <https://doi.org/10.1016/j.ecolind.2019.105874> (2020).
43. Jinfeng Wang, C. X. Geodetector: principle and prospective. *Acta Geogr. Sin.* **72**, 116–134. <https://doi.org/10.11821/dlxb201701010> (2017) (in Chinese).
44. Yuan, Y., Wang, R., Niu, T. & Liu, Y. Using street view images and a geographical detector to understand how street-level built environment is associated with urban poverty: A case study in Guangzhou. *Appl. Geogr.* **156**, 102980. <https://doi.org/10.1016/j.apgeog.2023.102980> (2023).
45. Song, Y., Wang, J., Ge, Y. & Xu, C. An optimal parameters-based geographical detector model enhances geographic characteristics of explanatory variables for spatial heterogeneity analysis: Cases with different types of spatial data. *GISci. Remote Sens.* **57**, 593–610. <https://doi.org/10.1080/15481603.2020.1760434> (2020).

46. Meng, X., Gao, X., Lei, J. & Li, S. Development of a multiscale discretization method for the geographical detector model. *Int. J. Geogr. Inf. Sci.* **35**, 1650–1675. <https://doi.org/10.1080/13658816.2021.1884686> (2021).
47. Faichia, C. et al. Using RS data-based CA-Markov model for dynamic simulation of historical and future LUCC in Vientiane. *Laos. Sustain.* **12**, 8410. <https://doi.org/10.3390/su12208410> (2020).
48. Li, Z., Zhou, Z., Liu, Z., Si, J. & Ou, J. Assessment and dynamic prediction of green space ecological service value in Guangzhou City China. *Remote Sens.* **16**, 4180. <https://doi.org/10.3390/rs16224180> (2024).
49. Shao-feng, R. & Ru-hui, M. Evaluation, spatial analysis and prediction of ecological environment vulnerability of Yellow River Basin. *J. Nat. Resour.* **37**, 1722–1734. <https://doi.org/10.31497/zrzyxb.20220705> (2022).
50. Zhang, Z., Hu, B., Jiang, W. & Qiu, H. Identification and scenario prediction of degree of wetland damage in Guangxi based on the CA-Markov model. *Ecol. Ind.* **127**, 107764. <https://doi.org/10.1016/j.ecolind.2021.107764> (2021).
51. Huang, Q. *China's industrialization process*. (Springer, 2018).
52. Pan, Z., Gao, G. & Fu, B. Spatiotemporal changes and driving forces of ecosystem vulnerability in the Yangtze River Basin, China: Quantification using habitat-structure-function framework. *Sci. Total Environ.* **835**, 155494. <https://doi.org/10.1016/j.scitotenv.2022.155494> (2022).
53. Wu, J., Zhang, Z., He, Q. & Ma, G. Spatio-temporal analysis of ecological vulnerability and driving factor analysis in the Dongjiang River Basin, China, in the Recent 20 Years. *Remote Sens.* **13**, 4636. <https://doi.org/10.3390/rs13224636> (2021).
54. Province, D. o. N. R. o. H. *Hebei Province Territorial Spatial Ecological Restoration Plan (2021–2035)*, <<https://zrzy.hebei.gov.cn/hb/gongk/gkml/zcwj/zcfgk/zck/10817092210285613056.html>> (2022).
55. Online, P. s. D. Ministry of Finance: During the 13th Five-Year Plan period, the central government invested 877.9 billion yuan to support ecological protection and restoration, <<http://finance.people.com.cn/n1/2020/1217/c1004-31970139.html>> (2020).

Acknowledgements

We would like to thank the anonymous reviewers for their constructive suggestions and comments.

Author contributions

Y.L. wrote the main manuscript text, W.X. assisted in reviewing and revising the manuscript, D.Z. helped secure funding support, and K.S. and Q.W. prepared all the figures. All authors reviewed the manuscript.

Funding

This research was funded by the geological survey projects of the China Geological Survey Bureau (grant number: DD20242329 and DD20243170).

Declarations

Competing interests

The authors declare no competing interests.

Additional information

Correspondence and requests for materials should be addressed to Y.L. or D.Z.

Reprints and permissions information is available at www.nature.com/reprints.

Publisher's note Springer Nature remains neutral with regard to jurisdictional claims in published maps and institutional affiliations.

Open Access This article is licensed under a Creative Commons Attribution-NonCommercial-NoDerivatives 4.0 International License, which permits any non-commercial use, sharing, distribution and reproduction in any medium or format, as long as you give appropriate credit to the original author(s) and the source, provide a link to the Creative Commons licence, and indicate if you modified the licensed material. You do not have permission under this licence to share adapted material derived from this article or parts of it. The images or other third party material in this article are included in the article's Creative Commons licence, unless indicated otherwise in a credit line to the material. If material is not included in the article's Creative Commons licence and your intended use is not permitted by statutory regulation or exceeds the permitted use, you will need to obtain permission directly from the copyright holder. To view a copy of this licence, visit <http://creativecommons.org/licenses/by-nc-nd/4.0/>.

© The Author(s) 2025